The Meteoritical Society

Meteoritics & Planetary Science 50, Nr 8, 1449–1467 (2015)
doi: 10.1111/maps.12480

Exploring the Moon's surface for remnants of the lunar mantle 1. Dunite xenoliths in mare basalts. A crustal or mantle origin?

Charles K. SHEARER[1,*], Paul V. BURGER[1], Aaron S. BELL[1], Yunbin GUAN[2], and Clive R. NEAL[3]

[1]Institute of Meteoritics, Department of Earth and Planetary Sciences, University of New Mexico, Albuquerque, New Mexico 87131, USA
[2]Division of Earth and Planetary Sciences, California Institute of Technology, Pasadena, California 91126, USA
[3]Department of Civil & Environmental Engineering & Earth Sciences, University of Notre Dame, Notre Dame, Indiana 46556, USA
[*]Corresponding author. E-mail: cshearer@unm.edu

(Received 17 November 2014; revision accepted 10 May 2015)

Abstract–Remotely sensed observations from recent missions (e.g., GRAIL, Kaguya, Chandrayaan-1) have been interpreted as indicating that the deep crust and upper mantle are close to or at the lunar surface in many large impact basins (e.g., Crisium, Apollo, Moscoviense). If this is correct, the capability of either impact or volcanic processes to transport mantle lithologies to the lunar surface should be enhanced in these regions. Somewhat problematic to these observations and interpretations is that examples of mantle lithologies in the lunar sample collection (Apollo Program, Luna Program, lunar meteorites) are at best ambiguous. Dunite xenoliths in high-Ti mare basalt 74275 are one of these ambiguous examples. In this high-Ti mare basalt, olivine occurs in three generations: olivine associated with dunite xenoliths, olivine megacrysts, and olivine microphenocrysts. The dunite xenoliths are anhedral in shape and are generally greater than 800 μm in diameter. The interior of the xenoliths are fairly homogeneous with regard to many divalent cations. For example, the Mg# (Mg/Mg + Fe × 100) ranges from 82 to 83 in their interiors and decreases from 82 to 68 over the 10–30 μm wide outer rim. Titanium and phosphorus X-ray maps of the xenolith illustrate that these slow diffusing elements preserve primary cumulate zoning textures. These textures indicate that the xenoliths consist of many individual olivine grains approximately 150–200 μm in diameter with low Ti, Al, and P cores. These highly incompatible elements are enriched in the outer Fe-rich rims of the xenoliths and slightly enriched in the rims of the individual olivine grains. Highly compatible elements in olivine such as Ni exhibit a decrease in the rim surrounding the xenolith, an increase in the incompatible element depleted cores of the individual olivine grains, and a slight decrease in the "interior rims" of the individual olivine grains. Inferred melt composition, liquid lines of descent, and zoning profiles enable the reconstruction of the petrogenesis of the dunite xenoliths. Preservation of primary magmatic zoning (Ti, P, Al) and lack of textures similar to high-pressure mineral assemblages exhibited by the Mg-suite (Shearer et al. 2015) indicate that these xenoliths do not represent deep crustal or shallow mantle lithologies. Further, they are chemically and mineralogically distinct from Mg-suite dunites identified from the Apollo 17 site. More likely, they represent olivine cumulates that crystallized from a low-Ti mare basalt at intermediate to shallow crustal levels. The parent basalt to the dunite xenolith lithology was more primitive than low-Ti basalts thus far returned from the Moon. Furthermore, this parental magma and its more evolved daughter magmas are not represented in the basalt sample suite returned from the Taurus-Littrow Valley by the Apollo 17 mission. The dunite xenolith records several episodes of crystallization and re-equilibration. During the last episode of re-equilibration, the dunite cumulate was sampled by the 74275 high-Ti basalt and transported over a period of 30–70 days to the lunar surface.

INTRODUCTION

After decades of searching, samples of the Moon's mantle have not been unambiguously identified in lunar materials returned by the Apollo or Luna programs, or in lunar meteorites. The lack of mantle materials in these collections has been partially attributed to dramatic differences in the nature of tectonic and volcanic activity on Earth compared to the Moon (e.g., Basaltic Volcanism Study Project 1981; Papike et al. 1998). Unlike the Moon, the Earth has plate tectonic processes which transport mantle materials (e.g., alpine peridotites, ophiolites, abyssal peridotites) to the planet's surface (e.g., Quick 1981; Moores 1982). Terrestrial magmatism provides another mechanism to transport xenoliths of numerous mantle mineral assemblages to the Earth's surface (e.g., Basaltic Volcanism Study Project 1981). Differences in basalt composition (volatile content and composition, viscosity, density), styles of magma transport and eruptive processes, and gravity (e.g., Day and Taylor 2007) between the Earth and Moon may be responsible for the apparent absence of xenoliths in lunar basalts. In addition to distinctly different tectonic and volcanic processes on the Earth and Moon, the apparent lack of mantle-derived lunar samples could also be attributed to a thick and ancient crust, or unrepresentative sampling of the lunar surface by humans and meteorites.

While terrestrial-style geologic processes on the Moon may not be available to bring mantle material to the surface, there are geologic regions of the lunar surface that may provide access to samples from the mantle. Due to large basin-forming events, the lunar mantle may have been mechanically transported to the surface or the lunar crust had been thinned to such a great extent that mare magmatism associated with these basins may have been able to transport mantle xenoliths to the surface. Using both gravity and topography data to develop crustal thickness models, Wieczorek and Phillips (1998) predicted the lunar mantle may be exposed in several basins (e.g., Crisium, Apollo). Interpretation of more recently collected gravity data from the NASA GRAIL (Gravity Recovery and Interior Laboratory) mission suggests that the thickness of the lunar crust varies from a high of approximately 60 km in the farside highlands to a low of less than 1 km within numerous impact basins (Wieczorek et al. 2013; Miljkovic et al. 2015). X-ray fluorescence data obtained from lunar orbit by the Apollo program over craters that penetrated the Crisium basin have been interpreted to indicate the excavation of Mg-rich basalt flows, underlying mantle, or an impact melt sheet with a mantle component (Andre et al. 1978; Wieczorek and Phillips 1998; Wieczorek et al. 2006; Miljkovic et al. 2015). The Kaguya and Chandrayaan-1 missions identified olivine, exposed and clustered at the surface near Crisium on the nearside and Moscoviense on the farside, as well as a few smaller basins within the South Pole–Aitken basin on the farside. One interpretation of these observations is that in some of the basins, mantle material may be exposed at the surface (Yamamoto et al. 2010; Miljkovic et al. 2015). Melosh et al. (2014) argued that the upper lunar mantle is dominated by orthopyroxene (+olivine) and that large impact basins such as the South Pole–Aitken basin excavated a large mass of mantle-derived orthopyroxene-bearing lithologies over the lunar highlands. A similar upper mantle mineralogy consisting of olivine-bearing pyroxenites was proposed by Kuskov et al. (2015) based on seismic models. With remotely sensed observations indicating the likelihood for deep crust and mantle mineral assemblages being proximal to or exposed at the lunar surface, it is timely to re-examine materials collected during sample return missions and within the lunar meteorite collection to explore the potential for the transport (impact or volcanic) of the lunar mantle to the surface of the Moon.

Only a few returned lunar samples are suspected to originate from either the deep crust or upper mantle. Spinel troctolites are inferred to have crystallized at depths of 15–25 km, whereas chromite–augite–orthopyroxene symplectites in troctolites and dunites indicate crystallization conditions equivalent to 45–50 km (e.g., Marvin et al. 1989; McCallum and Schwartz 2001; Shearer et al. 2015). These estimated depths approach the base of the crust as implied by the interpretation of GRAIL data and provide fundamental evidence for the potential for mantle rocks to be transported to the lunar surface. There are several examples from other petrologic studies that identified monomineralic Mg-rich olivine or unusual pyroxenes, the origins of which remain enigmatic. Ryder and Marvin (1978), Basu et al. (1978), and Blanchard et al. (1978) dissected Luna 24 samples collected at Mare Crisium and identified mineralogical components that could represent the high Mg component referred to by Andre et al. (1978), Wieczorek and Phillips (1998), and Wieczorek et al. (2006, 2013). Spudis et al. (1991) and Ryder et al. (1997) identified individual olivine grains in impact-generated poikilitic melt breccias (Apollo 15 and 17 missions) that they speculated could be either from Mg-suite lithologies or a component of the lunar mantle. Beaty and Albee (1980) reported a pyroxenite xenolith in the Apollo 11 high-Ti basalts and suggested that the pyroxene composition reflected a very high-pressure mineral assemblage of possible mantle origin. Dunite clasts occur in breccias collected from the Apollo 17 landing site. These dunite clasts (72415,

72416, 72417, 72418) range in mass from 3.55 to 32.34 g. It was initially speculated that these dunites represented a lithology from the lunar mantle (Bell and Mao 1975), but these lithologies are now considered to be Mg-suite lithologies, formed through olivine accumulation in either near-surface (Ryder 1992) or deep crustal (Shearer et al. 2015) environments. Ryder's (1992) consideration for a hypabyssal origin for this dunite lithology was based on the Ca content of the olivine which had been linked to depth of origin (Simkin and Smith 1970), although more recent studies illustrate the complexity of this interpretation (e.g., Kohler and Brey 1990). In the 74275 high-Ti mare basalt, dunite xenoliths have been identified (Walker et al. 1973; Meyer and Wilshire 1974; Delano and Lindsley 1982). The 74275 basalt was collected adjacent to gas-driven, pyroclastic deposits represented by the Apollo 17 orange volcanic glass. The origin of these dunitic xenoliths is particularly fascinating in light of continued speculation that peridotitic xenoliths from mantle or midcrustal magma chambers may be associated with basaltic magmas erupted in a variety of geologic settings unsampled by Apollo such as maar-style volcanoes, rims of small craters, and massifs on the rims of large craters (e.g., McGetchin and Ullrich 1973; Powell et al. 2012; Corley et al. 2014). As part of an extensive study to reassess previous identification of xenoliths (Walker et al. 1973, 1975a, 1975b, 1976; Meyer and Wilshire 1974; Beaty and Albee 1980; Delano and Lindsley 1982) and explore the potential for mantle components on the lunar surface, we examined the dunite xenoliths in high-Ti basalt 74275 in much more detail than previous studies. These fragments potentially represent a mineral assemblage from one of the following sources (1) the lunar mantle, (2) shallow- to midcrustal level cumulates from mare magmas, or (3) deep crustal level cumulates representing the Mg-suite magmas, or cognate cumulates.

DESCRIPTION AND PETROGENESIS OF HOST MAGMAS FOR THE DUNITE XENOLITHS

Apollo 17 High-Ti Basalts

The Apollo 17 high-Ti basalts are all low-K and have similarities to the high-Ti, low-K basalts from the Apollo 11 site (Neal and Taylor 1992). Early on, the Apollo 17 high-Ti basalts were distinguished from one another based on petrographic differences (Duncan et al. 1974; Papike et al. 1974; Brown et al. 1975; Warner et al. 1975; Walker et al. 1976). These three studies classified the basalts as: Type 1A basalt, rich in olivine megacrysts within a quenched textured groundmass; Type 1B basalt, which is olivine-poor with poikilitic plagioclase in a coarse-grained matrix; and Type II olivine-free, low-Mg basalt, which is similar to the Apollo 11 low-K basalts.

These basalts have been classified into five basalt types based on geochemistry. Rhodes et al. (1976) differentiated the Apollo high-Ti basalts into groups A, B, and C. Although Types A and B have similar major element characteristics, Type A basalts contain 50–60% higher incompatible trace element abundances than Type B. Neal et al. (1990) demonstrated that the Type B basalts could be subdivided into B1 and B2 based on rare earth element (REE) data. Type C has similar incompatible trace element abundances as Type A, but it has higher MgO and Cr_2O_3. The high MgO is reflected in the higher Fo content of the olivine. Ryder (1988, 1990) identified an Apollo 17 high-Ti basalt that had lower REE and a deeper Eu anomaly than the B types, but is more MgO- and Cr_2O_3-rich and Ca- and TiO_2-poor than other Apollo 17 basalts. He referred to this basalt as Type D, although Neal and Taylor (1992, 1993) disputed whether this was really a new basalt type. Within this classification, the Apollo 17 orange glasses have trace element characteristics similar to the Type B high-Ti basalts, but are distinctly different based on combined trace and major element characteristics (Neal et al. 1990). Sample 74275 has been classified as a Type C, Apollo 17 basalt (Paces et al. 1991).

High-Ti Basalt 74275

Basalt 74275 has been described in great detail by Meyer and Wilshire (1974), Hodges and Kushiro (1974), Brown et al. (1975), Delano and Lindsley (1982), Neal and Taylor (1993), and the lunar sample compendium (http://curator.jsc.nasa.gov/lunar/lsc/74275.pdf). The high-Ti basalt consists of large crystals of olivine (up to 0.7 mm), pink pyroxene (up to 0.5 mm), and ilmenite/armalcolite laths (up to 0.7 mm in length) in a subvariolitic groundmass of plagioclase, pyroxene, ilmenite, tridymite, glass, iron metal (<1 wt% Ni), and troilite. Olivine occurs in at least three generations (Delano and Lindsley 1982): olivine associated with dunitic xenoliths, olivine megacrysts, and olivine microphenocrysts (Fig. 1). Small euhedral chromites are found as xenoliths in the olivine clusters (Neal and Taylor 1993). Some of the olivine phenocrysts are rimmed with pyroxene. All pyroxene is high-Ca pyroxene with substantial TiO_2 (6.8 wt%). Sung et al. (1974) proposed that a substantial amount of the Ti in the pyroxenes was trivalent. The large laths of Fe-Ti oxides consist of armalcolite rimmed with ilmenite (El Goresy et al. 1974; Hodges and Kushiro 1974). A compilation of the geochemistry of 74275 Apollo 17 is presented in lunar sample compendium (http://curator.jsc.nasa.gov/lunar/lsc/74275.pdf). Longhi (1987,

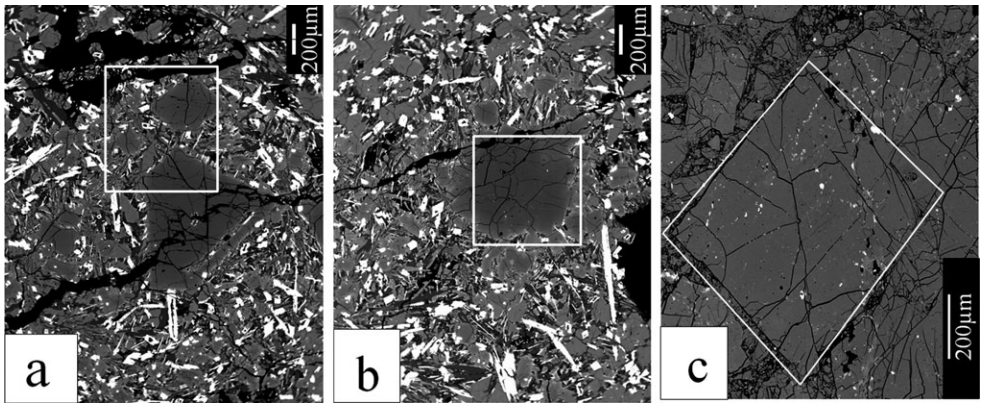

Fig. 1. BSE images of 74275,97 (high-Ti mare basalt) and 72415,55 (dunite clast in breccia). Sample 74275 is a high-Ti mare basalt with multigenerational olivines. Olivine occurs: a) in the groundmass of the basalts and as megacrysts that appear to not be in equilibrium with the basaltic melt. b) Xenoliths are dunites. c) Sample 72415 represents coarse-grain dunite of plutonic origin that occurs as a clast in lunar breccias. The dunite clast is not related to mare basaltic magmatism, but is a member of the Mg-suite (e.g., Ryder 1992). Scale bars for the three images are 200 μm in length. Area for X-ray maps in Fig. 2 are outlined in white.

1992) argued that the 74275 basalts are not related to the Apollo 17 orange volcanic glasses through fractional crystallization.

Murthy and Coscio (1977) dated 74275 at 3.77 ± 0.08 Ga using the Rb-Sr chronometer. Nyquist et al. (1976) obtained an age of 3.73 ± 0.32 Ga. Nunes et al. (1974) and Paces et al. (1991) determined whole rock U-Th-Pb and Sm-Nd isotopes, respectively. The Ar-Ar ages (Huneke et al. 1973; Husain and Schaeffer 1973) derived for the eruption of the Apollo 17 orange glass are between 3.48 ± 0.05 and 3.65 ± 0.06 Ga. These ages have been recalculated from original manuscripts using updated decay constants. Based on all of the chronology for the Apollo 17 basalts, Taylor et al. (1991) concluded that the Apollo 17 orange glass is slightly younger than the crystalline mare basalts. The crystallization age of the dunitic xenolith has not been determined.

ANALYTICAL APPROACH

Electron Microprobe Imaging and Analysis

Thin sections of high-Ti mare basalt 74275(96, 97), and Mg-suite dunite 72415,55 were initially examined and documented using backscattered electron imaging (BSE) on the JEOL JXA-8200 Superprobe electron microprobe (EMP) in the Institute of Meteoritics at the University of New Mexico (UNM). Sample 72415 was selected to compare the olivine in Mg-suite dunite (e.g., Ryder 1992; Shearer et al. 2015) to the dunitic xenoliths in 74275. Once suitable areas were located through BSE, wavelength-dispersive (WDS) X-ray maps were collected for Cr, Ca, Mn, P, and Ti, while energy-dispersive (EDS) maps were collected for Mg and Fe. Maps were collected using a 15 kV accelerating voltage, a 500 nA beam current, and a dwell time of 800 ms pixel^{-1}. Quantitative analyses were conducted as traverses, from core to rim of a dunitic xenolith, olivine megacrysts, and olivine microphenocrysts using the EMP. The point analyses employed an accelerating voltage of 15 kV, a beam current of 20 nA, and a spot size varying from 1 to 3 μm. Standards for the olivine point analyses consisted of a suite of C.M. Taylor Company mineral and synthetic standards, as well as select, in-house mineral standards. Stoichiometric constraints were used to determine the quality of the EMP analyses, and detection limits were calculated at the 3σ level. To more accurately determine the concentration and variability of Ti and V in the olivine, these two elements were analyzed separately in the trace element mode. The Ti and V data were empirically corrected and incorporated into the complete EMP analysis. The intensity of the Ti K_{Beta} peak relative to Ti K_{Alpha} was determined in a V-free sample. By measuring Ti K_{Alpha} in the unknown, this ratio can be applied to determine and subtract the contribution of the Ti K_{Beta} overlap onto V $K_{Alpha.}$ All usual corrections (e.g., ZAF) were made as well. The analyses were conducted using the same accelerating voltage, beam current, and a spot size as above, but counting times (for both peak and background) were extended to 200 s (rather than 30 s on the peak, and 15 s on background, in the above analysis). This resulted in an improvement in the 3σ detection limit to 39 ppm for Ti and 33 ppm V for olivine. A summary of results of the EMP data for olivine are presented in Table 1.

Table 1. Olivine analyses for microphenocrysts, megacrysts, and xenoliths in 74275, 97, and dunite clast from 72415.

Sample specific data point	74275 ,97 average	74275 ,97 Ol2-T1-23	74275 ,97 Ol2-T1-2	74275 ,97 OlX-T1-28	74275 ,97 OlX1-T1-40	74275 ,97 OlX1-T1-1	72415 ,55 T1-40	72415 ,55 T1-3
Olivine type	Microphenocryst core	Megacryst core	Megacryst rim	Dunite xenolith olivine core	Dunite xenolith olivine rim	Dunite xenolith rim	Mg-suite dunite olivine core	Mg-suite dunite olivine rim
SiO_2	38.18	39.02	37.35	39.13	38.95	37.51	40.16	40.30
TiO_2	0.13	0.12	0.20	0.02	0.05	0.10	0.01	0.01
Al_2O_3	0.07	0.06	0.06	0.04	0.06	0.06	0.04	0.00
Cr_2O_3	0.29	0.29	0.21	0.26	0.24	0.16	0.01	0.01
V_2O_3	0.01	0.01	0.01	0.01	0.01	0.01	0.01	0.01
FeO	21.68	19.35	26.07	15.93	16.39	28.30	11.30	11.29
MgO	38.66	41.16	36.05	44.38	43.81	34.05	48.09	48.29
MnO	0.25	0.20	0.32	0.16	0.20	0.33	0.11	0.10
CaO	0.28	0.24	0.33	0.26	0.25	0.32	0.10	0.11
P_2O_5	0.03	0.00	0.03	0.01	0.00	0.03	0.00	0.00
Total	99.57	100.46	100.63	100.19	99.95	100.86	99.84	100.11
Cation totals for four oxygen								
Tetrahedral site								
Si	0.996	0.996	0.986	0.987	0.987	0.997	0.993	0.994
Al	0.002	0.002	0.002	0.001	0.002	0.002	0.001	0.000
Ti	0.002	0.002	0.004	0.000	0.001	0.001	0.000	0.000
Total (T)	1.000	1.000	0.992	0.988	0.990	1.000	0.994	0.994
Octahedral site								
Al	0.000	0.000	0.000	0.000	0.000	0.000	0.000	0.000
Ti	0.001	0.000	0.000	0.000	0.000	0.001	0.000	0.000
Cr	0.006	0.006	0.004	0.005	0.005	0.003	0.000	0.000
V	0.000	0.000	0.000	0.000	0.000	0.000	0.000	0.000
Fe	0.473	0.413	0.576	0.336	0.347	0.629	0.234	0.233
Mg	1.504	1.567	1.419	1.669	1.655	1.349	1.773	1.773
Mn	0.006	0.004	0.007	0.003	0.004	0.008	0.002	0.002
Ca	0.008	0.007	0.009	0.007	0.007	0.009	0.003	0.003
Total (O)	1.998	1.997	2.015	2.020	2.018	1.999	2.012	2.011
TOTAL (O+T)	2.998	2.997	3.007	3.008	3.008	2.999	3.006	3.005
%Fo	76.1	79.1	71.1	83.2	82.7	68.2	88.3	88.4

Secondary Ion Mass Spectrometry Analysis

Trace elements (Al, Ti, V, Co, Ni, Y) in the olivine from the dunitic xenolith were analyzed by secondary ion mass spectrometry (SIMS) by combining data collected from the Cameca Nano-SIMS-50L at California Institute of Technology with data produced using the Cameca ims 4f SIMS at UNM. The high spatial resolution offered by the Cameca Nano-SIMS-50L was used to provide well-defined traverses across individual olivine grains making up the dunitic xenolith, whereas the Cameca ims 4f was used to provide additional calibration of the nano-SIMS data by providing analyses in large homogeneous areas of the olivine. The EMP X-ray maps and quantitative spot analyses were used to position traverses for nano-SIMS trace element analyses at high spatial resolution. Thin sections of 74275 and UNM SIMS standard blocks with well-documented silicate standards such as olivine, orthopyroxene, and high-Ca pyroxene (Shimizu et al. 1978; Shearer and Papike 2005; Shearer et al. 2013) were simultaneously coated with carbon to produce identical carbon coat thicknesses. The carbon coat was tested for conductivity with a multimeter. The olivine was analyzed with a 2×2 μm O^- beam of ~300 nA and 12 KeV impact energy. Analyses were taken every 3–5 μm. Approximately 40 trace element analyses were performed on the olivine making up the 74275 dunitic xenoliths. Secondary cations of ^{27}Al, ^{28}Si, ^{47}Ti, ^{51}V, ^{59}Co, ^{62}Ni, and ^{89}Y were simultaneously collected with electron multipliers (EMs) at high mass resolution. The mass resolving power (MRP) was determined using the Cameca definition, which relates mass line width to mass dispersion by dividing the mass (M) of the isotope of interest by the total range in mass differences (ΔM)

among ions entering an electron multiplier. Masses were selected to minimize interferences. For every analysis point in the standards and unknowns, the intensities for each mass were normalized to ^{28}Si and multiplied by the wt% SiO_2. Calibration curves were constructed using these values for the standards versus concentration. This calibration approach follows that documented in numerous ion microprobe studies (e.g., Shimizu et al. 1978; Shearer and Papike 2005; Shearer et al. [2008], and references within these manuscripts). These calibration curves were then used to calculate concentrations in the olivine crystal being analyzed. The precision values for measurements of ^{27}Al, ^{28}Si, ^{47}Ti, ^{51}V, ^{59}Co, and ^{62}Ni were better than 10%. The precision for ^{89}Y was better than 25%. Estimates for detection limits of the trace elements were approximately 1.0 ppm. The University of New Mexico Cameca ims 4f ion microprobe was used to analyze ^{27}Al, ^{30}Si, ^{47}Ti, ^{51}V, ^{59}Co, ^{60}Ni, and ^{89}Y in the olivine to compare against the nano-SIMS data on larger homogeneous areas (Shearer and Papike 2005; Shearer et al. [2013] and references within these manuscripts).

RESULTS

Olivine Texture

Three generations of olivine in 74275 have been described in previous studies (Walker et al. 1973; Meyer and Wilshire 1974; Delano and Lindsley 1982; Neal and Taylor 1992, 1993) (1) anhedral to subhedral microphenocrysts, (2) euhedral megacrysts, and (3) anhedral dunitic xenoliths. The olivine microphenocrysts are generally anhedral and range in grain size from <50 μm to approximately 300 μm (Figs. 1a and 1b). They are immersed in a subvariolitic, finer grained groundmass of armalcolite rimmed by ilmenite, plagioclase, titanaugite, tridymite, metallic iron, troilite, and glass, and commonly contain euhedral to subhedral inclusions of chromite. Pyroxene rims some of the olivine. The megacrysts are euhedral to subhedral and range in size between 300 and 800 μm. The olivine megacrysts contain minor melt inclusions and euhedral to subhedral inclusions of chromite in their outer rims. Fe-Ti oxides are intergrown with late-stage, Fe-rich olivine rims and radiate normal to the olivine growth surface (Fig. 1a). The dunitic xenoliths (Fig. 1b) are anhedral in shape and are generally greater than 800 μm. They have thin Fe-rich rims (10–30 μm). There are minor inclusions of Fe metal that are generally <2 μm in diameter. Smaller sulfides globules are associated with some of the Fe metal grains.

For comparison, we examined sample 72415, which is a dunite lithology with Mg-suite heritage that occurred as a clast in a breccia (e.g., Dymek et al. 1975; Ryder 1992; Shearer et al. 2015). The olivine in the clast occurs as subround to angular fragments immersed in a fine-grained granulated matrix of predominantly olivine (Fig. 1c). Minor phases associated with the olivine include pyroxene, plagioclase, troilite, Fe metal, chromite, and phosphates. Symplectite assemblages of chromite + high-Ca pyroxene, high-Ca pyroxene–troilite veining, and phosphate veining are associated with the olivine. Ryder (1992) suggested that this cumulate crystallized in a hypabyssal crustal environment based on Fe/Mg zoning and CaO content, but Shearer et al. (2015) suggested a deeper crustal origin based on symplectite assemblages and the complexities that of relating pressure with CaO content in olivine (e.g., Kohler and Brey 1990).

Olivine Major and Minor Element Zoning

A comparison of major and minor element characteristics and zoning style among the different olivines in 74275 and between the olivines in 74275 and the dunite represented by sample 72415 are illustrated in Figs. 2 and 3. Table 1 presents examples of olivine compositions from 74275 and 72415. The BSE images (Fig. 1a), Mg X-ray maps (Fig. 2a), and elemental traverses (Fig. 3a) of the megacrysts in 74275 illustrate that they have large, fairly homogeneous cores with thin reaction rims that are approximately 50 μm wide. The Mg# of the cores range from 77 to 79. The Mg# transitions from 77 at the outer core to 70 at the rim immediately adjacent to the surrounding matrix. X-ray maps for Ti and P do not show any internal zoning in the core. With decreasing Mg# from megacryst core to rim are increases in MnO (approximately 0.21 wt% in the core to >0.32 wt% at rim), TiO_2 (approximately 0.10 wt % in core to >0.16 wt% at rim), CaO (approximately 0.25 wt% in core to >0.32 wt% at rim), and decreases in Cr_2O_3 (approximately 0.30 wt% in core to <0.20 wt% at rim).

The dunitic xenolith contains olivine with similar zoning with respect to Mg#. The cores of the xenolith are fairly homogeneous with Mg#s exhibiting limited variations from 82 to 83. The Mg# decreases from 82 to 68 over the 50 μm wide rim (Figs. 1b, 2b, and 3b). In contrast to the megacrysts, the Ti and P X-ray maps of the xenolith illustrate that slow diffusing elements preserve primary cumulate zoning textures. These X-ray maps illustrate that the dunitic xenolith consists of many individual olivine grains with low Ti and P cores. Individual olivine grains making up the xenolith range from approximately 0.02 to 0.03 wt% TiO_2 and <0.008 wt% P_2O_5 in cores to greater than 0.1 wt% TiO_2 and >0.02 wt% P_2O_5 in rims (Fig. 3b; Table 1).

To test the possibility that the Mg-suite dunites (72415) that occur at the Apollo 17 landing site may be the source of the xenoliths in the basalt (Ryder 1992;

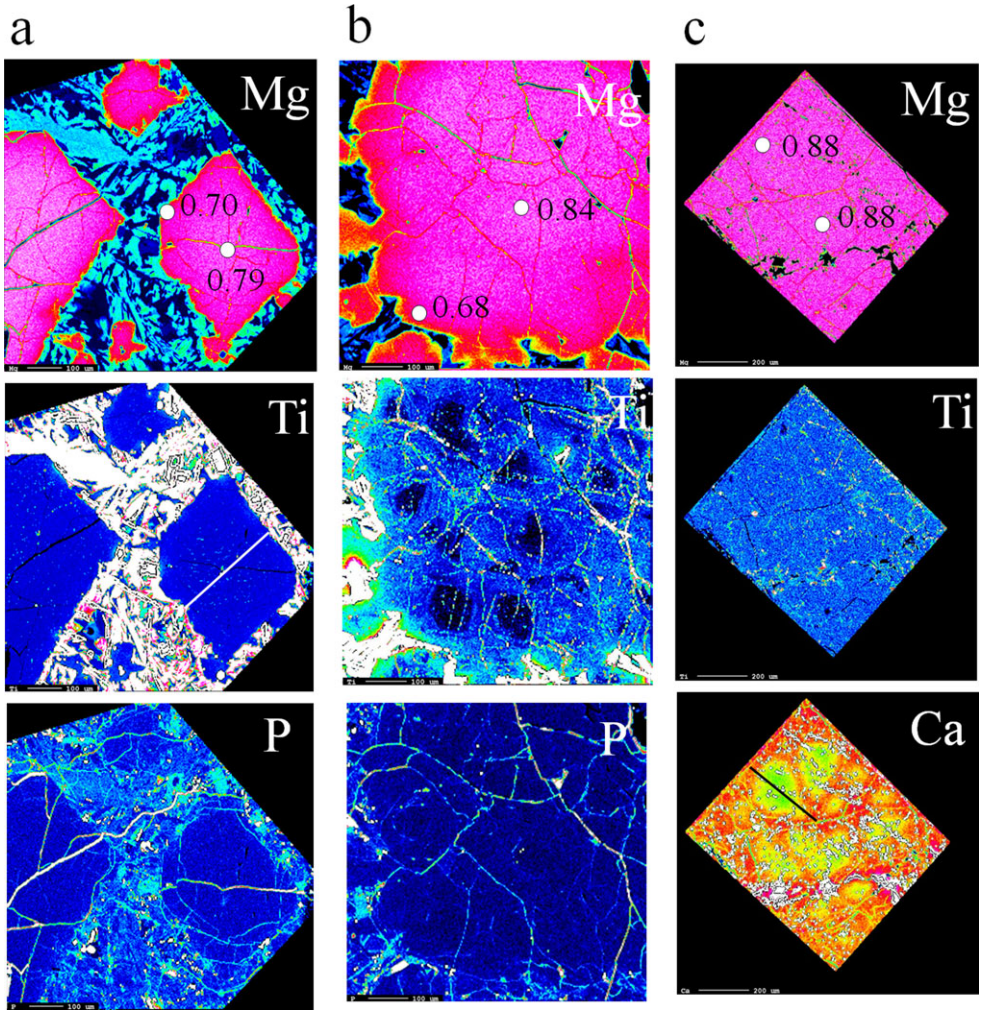

Fig. 2. High-current X-ray maps (Mg, Ti, and P or Ca) of (a) megacrysts, (b) dunite xenolith in 74275, and (c) olivine in the dunite clast in sample 72415. Mg# values are shown in the Mg maps. Phosphorous zoning is very subtle in the dunite xenolith and mimics Ti and does not occur at all in the olivine megacrysts. Phosphorous was not mapped in the dunite clast as P is very low in the olivine and appears to be concentrated in apatite veins cutting through the olivine (see fig. 14 in Shearer et al. 2015). The results of electron microprobe traverses are shown in Fig. 3. A nano-SIMS traverse across one of the dunite xenolith olivine crystals is located on the Ti map. The results of the nano-SIMS traverse are shown in Fig. 5.

Neal and Taylor 1993; Papike et al. 1998; Shearer and Papike 2005; Shearer et al. 2006, 2015), we examined the major and minor element zoning of the olivine in 72415. The BSE image, most X-ray maps, and spot analysis traverses across olivine of the dunite represented by sample 72415 (Figs. 1c, 2c, 3c, and 4) illustrate that the olivine is fairly homogenous with respect to Mg# (88.4–88.7), P_2O_5 (<0.005 wt%), MnO (0.10–0.13 wt%), Cr_2O_3 (0.01–0.03 wt%), and Ti (77–<33 ppm). In contrast to these elements, Ca appears to define an internal structure to these large olivine grains (Fig. 2c). These variations are subtle but low Ca cores of olivine fragments are approximately 0.05 wt% CaO, whereas the surrounding olivine reaches approximately 0.10 wt% CaO (Figs. 2c and 5).

Olivine Trace Elements

Trace element analyses collected by nano-SIMS are presented for selected spots across a portion of the olivine xenolith in 74275 (Fig. 5). The trace element variation across the traverse from the rim of the xenolith across one of the olivine grains making up the xenolith is shown in Figs. 2b and 6. Although the variation in Mg# does not reflect the subtle zoning defined by P and Ti (Figs. 2b and 3b), variations in Al, Ti, Ni, Co, and V clearly preserve a mixture of original cumulate texture as well as interactions between the xenolith and surrounding melt. The highly incompatible elements Al and Ti are enriched in the Fe-rich rim of the xenolith (320 and 1000 ppm, respectively), depleted

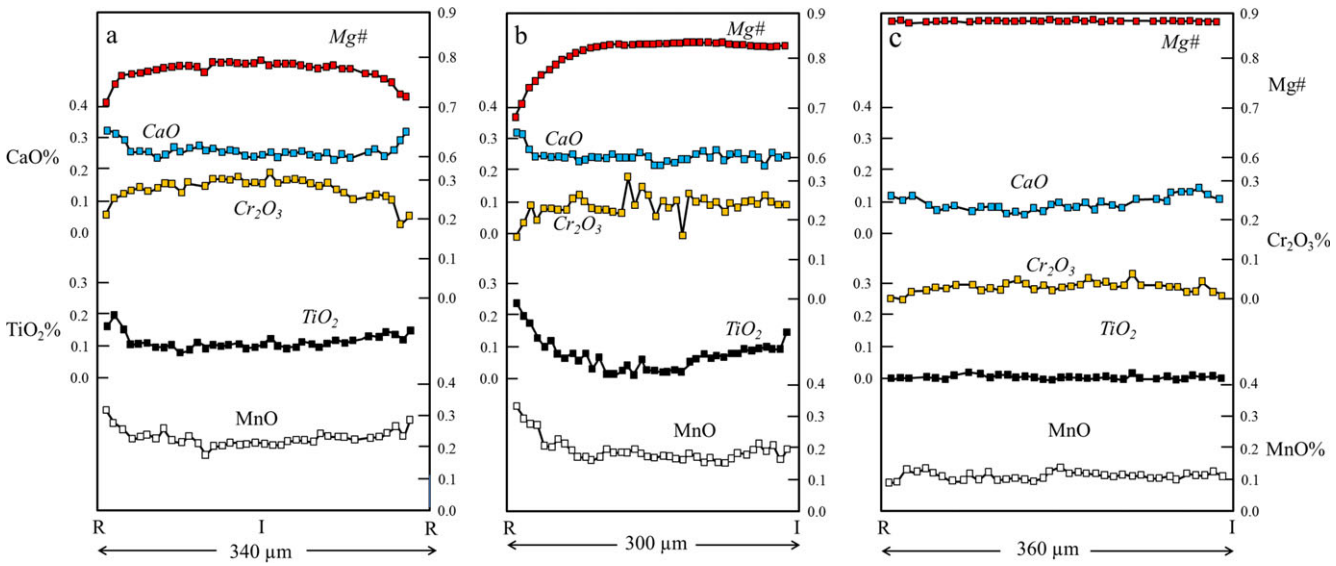

Fig. 3. Chemical variations in olivine between core and rim. a) Megacryst. b) Xenolith. c) Mg-suite dunite.

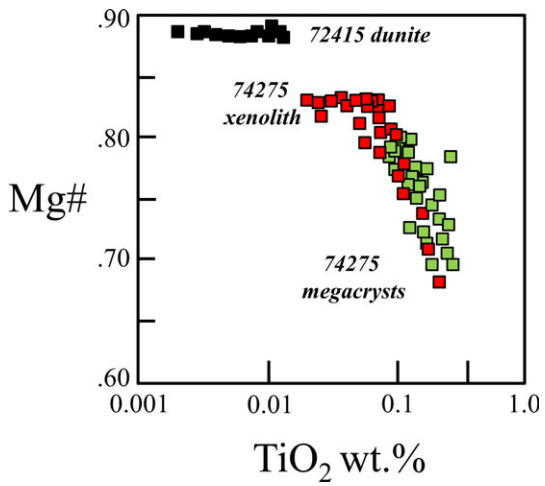

Fig. 4. Mg# versus TiO_2 for olivines present in 74275 and dunite xenolith in 72415.

in the core of the individual olivine grains making up the xenolith (100 and 300 ppm, respectively), and slightly enriched in the rims of individual olivine grains (140 and 500 ppm, respectively). The distribution of Ti as determined by nano-SIMS reproduces the observations made for the distribution of TiO_2 by EMP (Fig. 3b). Highly compatible elements in olivine such as Ni exhibit a decrease in the rim surrounding the xenolith (44 ppm), an increase in the incompatible element depleted (P, Al, Ti) core of the individual olivine grains making up the xenolith (133 ppm), and a slight decrease in the "interior rim" of the individual olivine grains (100 ppm). Moderately compatible element Co and moderately incompatible element V exhibit behavior contrasting with each other and highly compatible and incompatible elements. Cobalt is depleted in the core of individual olivine grains making up the xenolith (48 ppm) and is slightly higher in the rim of the xenolith (85 ppm) and the interior rim of the individual olivine grain (60 ppm). In contrast, V is enriched in the interior rim of the olivine (45 ppm), depleted in the core (34 ppm), and highly depleted in the xenolith rim (20 ppm).

DISCUSSION

Relationship between the Olivine Megacrysts and 74275

The olivine megacrysts in 74275 could potentially represent either an accumulation of an earlier generation of phenocrysts indigenous to the 74275-type magma or xenocrystic olivine introduced by mixing of another melt or solid component. To examine this relationship, we have calculated some compositional characteristics of the melt coexisting with the olivine megacrysts using both olivine–melt partitioning coefficients for minor and trace elements ($D^{olivine/melt}$) and Fe-Mg exchange coefficients ($K_D^{olivine/melt}$). Values for $D^{olivine/melt}$ and $K_D^{olivine/melt}$ used for calculating melt compositions are presented in Table 2. A similar approach is used later to estimate the composition of the melt in equilibrium with the olivine in the dunitic xenoliths. The selection of $D^{olivine/melt}$ for highly incompatible elements may contribute to errors in the calculated melt compositions; however, at the very least, this approach allows for a relative comparison among different generations of olivine in 74275.

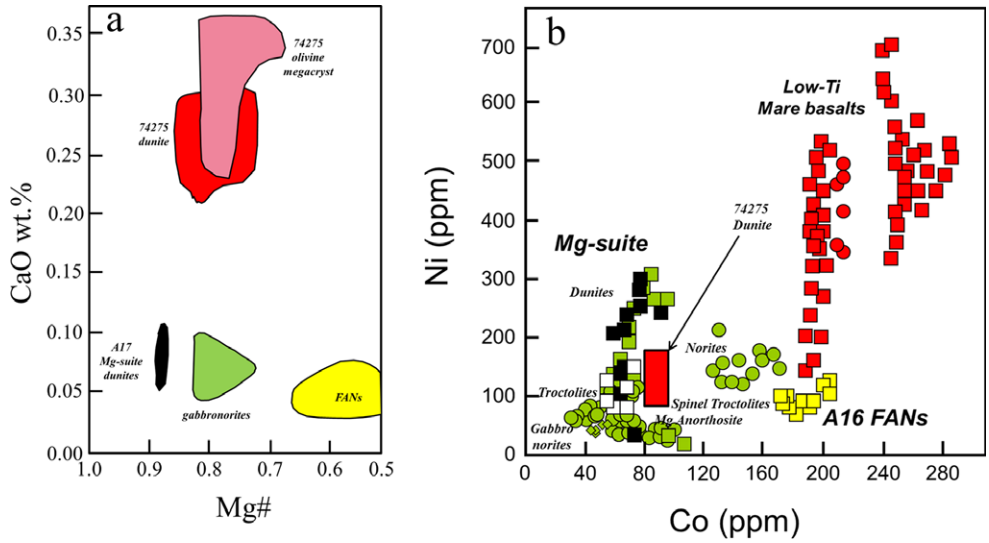

Fig. 5. Comparisons between different olivines from 74275 and olivine from other lunar lithologies. a) Mg# versus CaO. b) Co versus Ni.

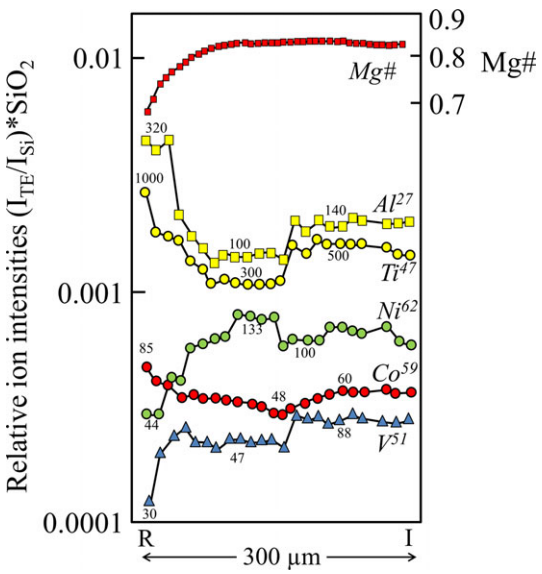

Fig. 6. A nano-SIMS traverse (see Fig. 2c) across one of the olivine crystals making up the dunitic xenolith. These are ion intensity values normalized to Si. For each element, these values are proportional to concentration.

TiO_2 was estimated for the melt in equilibrium with the cores of both the olivine microphenocrysts and olivine megacrysts. The TiO_2 was estimated using a $D_{Ti}^{olivine/melt}$ of 0.011 estimated for lunar basalts by Butler (1972) and Delano and Lindsley (1982). This value is similar to the $D_{Ti}^{olivine/melt}$ determined in a variety of experimental partitioning studies and analyses of natural occurring phenocryst–matrix pairs (0.007–0.015; Lindstrom 1983; Dunn 1987; Colson et al. 1988; McKenzie and O'Nions 1991; Nikogosian and Sobolev 1997). However, Longhi et al. (1978) reported significantly higher $D_{Ti}^{olivine/melt}$ (0.027–0.065) for a range of lunar bulk compositions (TiO_2 = 1.63–13.5 wt%) at various temperatures (1124–1375 °C) and pressures (12.5 kb). It is uncertain if the low concentrations of Ti in the olivine from their experiments compromise some of these discrepancies. Longhi et al. (1978) did not observe any relationship between $D_{Ti}^{olivine/melt}$ and melt composition, temperature, or pressure. Taura et al. (1998) used secondary ion mass spectrometry to examine Ti partitioning between olivine and melt at various pressures (3–14 GPa). Constructing Onuma diagrams for these data, they concluded that the $D_{Ti}^{olivine/melt}$ ranged between 0.008 and 0.026 (with an average of 0.014). Furthermore, they were unable to document any significant variation in the $D_{Ti}^{olivine/melt}$ with temperature or pressure. Using the $D_{Ti}^{olivine/melt}$ proposed by Butler (1972) and Delano and Lindsley (1982), the TiO_2 concentration of the melt in equilibrium with the microphenocrysts is approximately 12.6 wt% and the TiO_2 concentration of the melt in equilibrium megacrysts is 12.1 wt%. These values are similar to the bulk composition of 74275, which ranges from 12.6 to 13.1 wt% (Papike et al. 1976, 1998; Basaltic Volcanism Study Project 1981). Using the selected $D_{Ti}^{olivine/melt}$ appears to be internally consistent.

Using the TiO_2 content of the calculated magmas as a starting point, the Mg# for the parent melts to these two olivine populations were calculated. To calculate the Mg# for the parent melts from the olivine, it is necessary to know the TiO_2 of the melt, as Longhi et al. (1978), Delano (1980), and Longhi (1992) demonstrated that the Fe-Mg $K_D^{olivine/melt}$ depends on the TiO_2

Table 2. Ds and K_D used to calculate melt compositions from olivine analyses.

Elements	Value	References
Fe-Mg $K_D^{olivine/high\text{-}Ti\ melt}$	0.25	Longhi et al. (1978), Longhi (1992)
Fe-Mg $K_D^{olivine/low\text{-}Ti\ melt}$	0.32	Longhi et al. (1978), Longhi (1992)
$D_{Ti}^{olivine/melt}$	0.01	Butler (1972), Delano and Lindsley (1982), Mallmann and O'Neill (2009)
$D_{Cr}^{olivine/melt}$	0.75	Hanson and Jones (1998), Bell et al. (2014, unpublished data)
$D_{Ca}^{olivine/melt}$	0.033	Longhi et al. (1978), Mallmann and O'Neill (2009)
$D_{Mn}^{olivine/melt}$	0.83	Butler (1972), Longhi et al. (1978), Mallmann and O'Neill (2009)
$D_{Al}^{olivine/melt}$	0.0076	This article and based on Colson et al. (1988), Lindstrom (1983), Mallmann and O'Neill (2009)

concentration of the melt. The Delano (1980) data also showed that for the high-Ti basalt compositions, the Fe-Mg $K_D^{olivine/melt}$ increased by 0.01/kbar at least up to 20 kbars. Using the relationship between Fe-Mg $K_D^{olivine/melt}$ and TiO_2, a Fe-Mg $K_D^{olivine/melt}$ of 0.28 was used to calculate the Mg# of melts in equilibrium with the two populations of olivine. Using core olivine composition, the Mg# of melts in equilibrium with microphenocrysts and megacrysts are 46 and 50, respectively. The approximate Mg# for the bulk 74275 is approximately 50 and rather nicely agrees with the concept that the bulk rock is composed of melt plus added olivine.

To compare other chemical differences in potential parental melts between the microphenocrysts and megacrysts, olivine compositions were combined with appropriate $D^{olivine/melt}$ for Cr, Ca, Al, and Mn (Table 2). The $D_{Cr}^{olivine/melt}$ of 0.75 was used in these calculations based on the results of Hanson and Jones (1998), and Bell et al. (2014) for a temperature of 1250 °C and an fO_2 of IW-1. The modeling of Hanson and Jones (1998), Gaetani and Grove (1997), and Bell et al. (2014) is based upon a variety of basaltic melt (e.g., iron-rich Martian basalts, iron-free compositions) suggesting negligible effect in $D_{Cr}^{olivine/melt}$ with changes in bulk composition. The $D_{Ca}^{olivine/melt}$ of 0.030 used in this calculation is based on the experiments of Longhi et al. (1978). The values agree with observations and measurements of Butler (1972) for low-Ti mare basalts (0.032), and Dunn (1987) and Taura et al. (1998) for terrestrial basalts at a variety of pressures (0.034–0.035 and 0.033, respectively). Longhi et al. (1978) predicted a temperature dependency of $D_{Mn}^{olivine/melt}$. Using their equation for estimating the partitioning behavior of Mn between olivine and melt, the $D_{Mn}^{olivine/melt}$ at 1250 °C for mare basalts is 0.83. This is similar to values estimated by Butler (1972), Mikouchi et al. (1994), and Mallmann and O'Neill (2009) at lunar fO_2 conditions.

Based on these $D^{olivine/melt}$ values for Cr, Ca, Al, and Mn, the melt compositions calculated from the olivine microphenocrysts and megacrysts show important differences. The melt compositions calculated for the microphenocrysts are Cr_2O_3 = 0.38 wt%, CaO = 9.16 wt%, Al_2O_3 = 8.55 wt%, and MnO = 0.30 wt%. These values are similar to the bulk 74275 composition (e.g., Cr_2O_3 = 0.48–0.64 wt%, CaO = 10.38 wt%, Al_2O_3 = 8.51 wt%, and MnO = 0.25 wt%) particularly if a proportion of the olivine megacrysts are removed in calculating the true melt composition (Duncan et al. 1974). The melt compositions calculated for the megacrysts are Cr_2O_3 = 0.39 wt%, CaO = 7.93 wt%, Al_2O_3 = 7.76 wt%, and MnO = 0.24 wt%.

The relationship among these calculated magmas can be examined in the context of liquid line of descent (LLD) trajectories for MgO versus TiO_2, calculated by Longhi (1987). Figure 7 is a plot modified from Longhi's initial calculations and figures. This plot combines all of the mare basalt compositions considered by Longhi (1987) over the entire range of TiO_2. Unlike the diagram presented by Longhi (1987), the *x*-axis in Fig. 7 has been modified from MgO wt% to Mg#. This conversion was done by plotting pyroclastic glass and mare basalt compositions in the original plot and calculating Mg# from their bulk compositions. Bulk compositions that plotted on olivine or olivine + Fe-Ti oxide saturated LLD could easily be transferred into the Mg#-TiO_2 plot. Using this plot, it is clear that there are subtle differences observed between our calculated liquid compositions for the microphenocrysts and megacrysts, the bulk 74275 composition, and the parent melt composition calculated from the olivine megacrysts by Delano and Lindsley (1982). Of particular importance is that within the error of the analytical measurements and selected $D^{olivine/melt}$, the calculated compositions for the microphenocrysts and megacrysts plot on a similar LLD for Mg# and TiO_2. This similar LLD is also consistent with variations in incompatible elements, with CaO, Al_2O_3, and MnO increasing along this LLD. These data imply that the microphenocrysts and megacrysts both crystallized from high-Ti basaltic magmas with very similar compositions. The simplest interpretation is that these two types of olivine "phenocrysts" crystallized from the same parental high-Ti basalt under two different conditions.

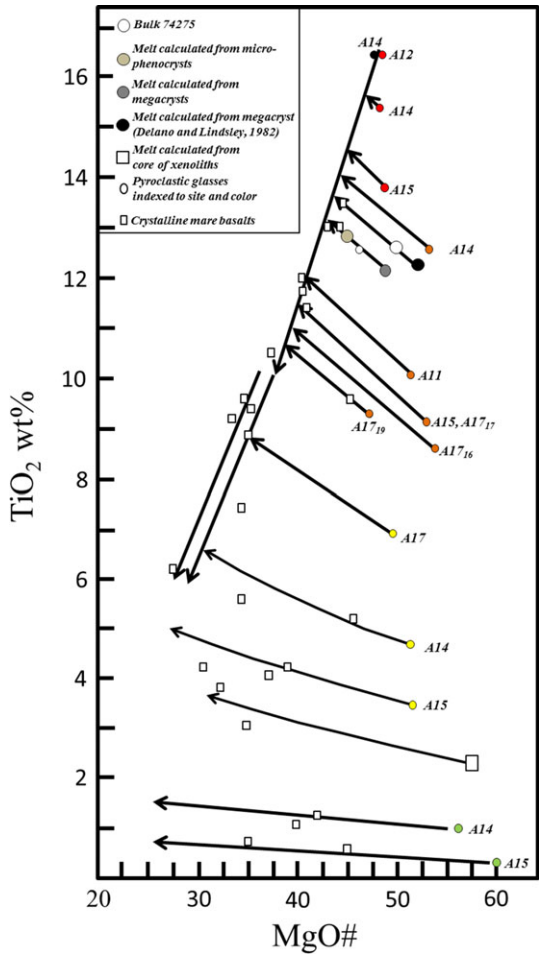

Fig. 7. Liquid lines of descent for mare basalts plotted in terms of Mg# versus TiO_2. This diagram combines the experiments and illustrations from Longhi (1987), but the *x*-axis has been converted to Mg#. Liquid compositions calculated from the three generations of olivine in 74275 are plotted along with their liquid lines of descent. The olivine microphenocryst and megacrysts define melts that lie along similar liquid lines of descent of a parent basalt for 74275. However, olivine in the dunite xenolith appears to define a different parent magma.

Petrogenesis and Transport of Olivine Megacrysts

A plethora of previous studies have attempted to extract the time scales and thermal histories of magmatic processes using zoning patterns observed in crystals (e.g., Bottinga et al. 1966; Lofgren 1972; Anderson 1983; Blundy and Shimizu 1991; Costa and Dungan 2005; Costa et al. 2008). In particular, modeling of zonation patterns in olivine has proven to be both highly interpretable and applicable for reconstructing both terrestrial and extraterrestrial magmatic processes (e.g., Donaldson 1976; Onorato et al. 1978; Armienti et al. 1994; Fagan et al. 2002; Costa and Dungan 2005; Miyamoto et al. 2006; Costa et al. 2008). The effectiveness of using olivine zoning in modeling magmatic processes (e.g., Chakraborty 2010; Qian et al. 2010; Spandler and O'Neill 2010) is the result of diffusion in olivine being well-documented (e.g., anisotropy of diffusion, diffusivities for many elements over a range of temperatures, exchange of major and minor elements between mineral and melt).

Based on the previous section, a likely scenario for the petrogenesis of the olivine megacryst in 74275 is that they crystallized in a magma chamber in the lunar crust, were homogenized during extended magmatic residence in the chamber, and were then transported and erupted on the lunar surface in the high-Ti 74275 magma. This is somewhat similar to the model suggested by Fagan et al. (2002) and Day and Taylor (2007) for the olivine megacrysts in lunar meteorite NWA 032. Using conditions that are also appropriate for the megacrysts in 74275 (cooling rate of 2 °C h^{-1}, liquidus temperature of 1220 °C, and a viscosity of 3 Pa-S), Fagan et al. (2002) estimated approximate growth rates for the olivine phenocrysts in NWA 032 of between 10^{-7} and 10^{-8} cm s^{-1}. In contrast, Day and Taylor (2007) calculated growth rates for the olivine in NWA 032 to be a bit slower, at approximately 3×10^{-9} cm s^{-1}. This range of growth rate values is similar to other estimates for the growth rates of silicates in basalts, between 10^{-8} and 10^{-9} cm s^{-1} (Cashman and Marsh 1988; Marsh 1998; Jerram et al. 2003). Using the slower rate, between 1×10^{-8} and 3×10^{-9} cm s^{-1} (proposed by Fagan et al. [2002] and Day and Taylor [2007]), it took between 115 and 385 days to grow the larger megacrysts (1 mm) in the magma chamber for the 74275 magma. Based upon the diffusion of Fe and Mg in olivine (Chakraborty 1997), these relatively long periods of olivine growth and residence in the magma chamber would result in the homogenization of the Fe and Mg. Fagan et al. (2002) calculated that the somewhat smaller NWA032 olivine megacrysts would have become homogenized with regard to their Fe-Mg within 40 days at temperatures of 1220 °C. The megacrysts from 74275 would have become homogenous within the growth time estimated above (between 115 and 385 days). An interesting difference between the megacrysts in 74275 and NWA 032 is that the megacrysts in NWA 032 have cryptic P zoning (Elardo and Shearer 2014), which is absent in the olivine megacrysts in 74275. It is unlikely that the lack of cryptic P zoning is simply the result of P zoning in the olivine being below the detection limit of the imaging as the P_2O_5 in 74275 parent (0.06–0.074 wt%) is only slightly less than that measured in NWA 032 (P_2O_5 = 0.09 wt%) (P_2O_5 data from Neal and Taylor 1993; Fagan et al. 2002). More likely, the longer residence time in the magma may have resulted in either limiting the formation of cryptic P zoning due to the kinetics of the olivine

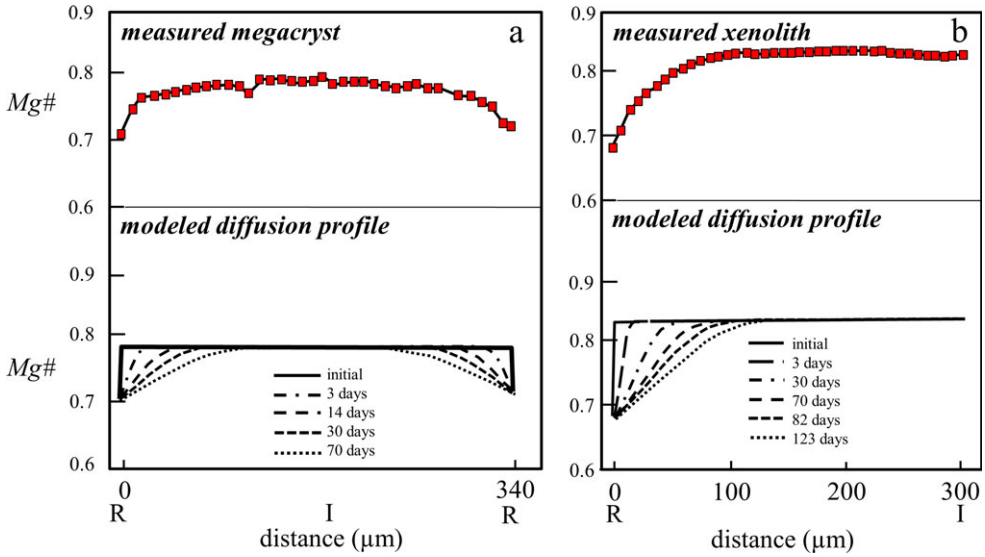

Fig. 8. Comparisons between measured Mg# profiles across olivine rims from a) megacryst in 74275 and b) dunite xenolith in 74275. Diffusion profiles are calculated using the worksheet created by Costa et al. (2008).

surface and melt or the P zoning may have been erased via diffusion (e.g., Qian et al. 2010).

It is our contention that the Fe-enrichment observed along the rim of the 74275 olivine megacrysts reflects the changing conditions that result from the transport of the 74275 magma from the magma chamber through the crust to the lunar surface. This interpretation is based on several observations. (1) Megacrysts are generally euhedral in shape, whereas adjacent microphenocrysts are subhedral, suggesting olivine growth in two different environments (Fig. 1a). (2) The Fe-enrichment in the megacrysts is associated with euhedral olivine surfaces suggesting diffusion across these surfaces rather than late-stage crystallization of olivine (Figs. 1a and 2a). (3) Potentially the same LLD for early olivine megacryst and late olivine microphenocrysts (Fig. 7). The diffusion time scale for the production of the Fe-enriched rim can be made by combining electron microprobe traverses across olivine megacrysts with worksheets for calculating diffusion profiles prepared and made available by Costa et al. (2008) (Chapter 14 of Reviews in Mineralogy and Geochemistry volume 69: http://www.minsocam.org/MSA/RIM/rim69.html). Calculations for the rate of transport of the megacrysts are based on (1) the olivine megacrysts are homogeneous with a composition of Fo_{78}, (2) the magma has a temperature of 1200 °C based on temperature–pressure experiments on 74275 by Green et al. (1975), and (3) the diffusion profile measured in the olivine is near parallel to [010] or [100]. Costa et al. (2008) illustrated that diffusion of Fe and Mg in olivine is anisotropic and that diffusion parallel to [001] is approximately six times faster than diffusion parallel to either [010] or [100]. A comparison between a measured diffusion profile for Fe-Mg across an olivine megacryst and calculated diffusion profiles for various periods of time is illustrated in Fig. 8a. The resulting modeling indicates that the Fe-enriched rim on the megacrysts formed over a period of 14–30 days. The Fe-enriched rim represents the period of time from basalt transport from the magma chamber, cooling at the surface, to the crystallization of plagioclase late in the crystallization sequence at 1130 °C (Green et al. 1975). If most of this diffusion profile was produced during the transport process and not during cooling of the lava flow on the lunar surface, the ascent rate of the megacrysts is substantially slower than mare basalt ascent rates previously proposed for the Moon (e.g., Wilson and Head 1981; Spera 1992).

Potential Source Lithologies for the Dunite Xenoliths

Potentially, the dunite xenoliths in 74275 could be related to the Apollo 17 dunites with a Mg-suite heritage, linked to mare basaltic magmatism at the Apollo 17 site as crustal accumulations of olivine (either directly linked to the high-Ti mare basalt represented by 74275 or another mare basalt type), or a lunar mantle lithology. Here, we explore these alternatives.

As dunites related to the Mg-suite were identified and collected at the Apollo 17 site approximately 3.0 km from the 74275 sample collection site, it makes sense to explore the possibility that these two dunite lithologies are related. The BSE images in Fig. 1 and the X-ray maps in Fig. 2 illustrate that there are significant textural differences between these two dunites. The Mg-suite dunite is substantially brecciated and has distinctly

different zoning compared to the dunite xenolith. However, the Mg-suite dunite has irregular Ca zoning; the 74275 dunite has well-defined zoning of Ti and P (and Al, V, and Ni) suggestive of an igneous origin. The Mg-suite dunite also has textures suggestive of a deep crustal origin such as chromite–pyroxene sympltectites as well as phosphate- and sulfide-pyroxene veining. These types of textures are reminiscent of textures observed in deep-seated crustal and mantle xenoliths on Earth (Basaltic Volcanism Study Project 1981). Although the olivine in the Mg-suite dunite has Co and Ni concentrations that overlap with those observed in the olivine in the 74275 dunitic xenoliths (Fig. 6b), the Mg-suite dunite has a higher Mg# (Figs. 3 and 4) and lower concentrations of Cr, Ti (Figs. 3 and 4), and Ca (Fig. 6a). Clearly, these two dunites are unrelated. Further, the textural data seem to imply that these two lithologies represent emplacement in two different crustal regimes, a deep crustal environment (Mg-suite dunite), and a hypabyssal crustal environment (dunitic xenoliths). These differences in texture also suggest that the 74275 xenoliths do not represent lithologies that were exposed for long durations to the pressure and temperature conditions of the deep crust or upper mantle. Therefore, it is unlikely that the xenoliths are derived from the lunar upper mantle.

To compare differences in parental melt between the olivines that crystallized from the 74275 basalt and the dunitic xenolith, olivine compositions from the dunitic xenolith were combined with appropriate Fe-Mg $K_D^{olivine/melt}$ and $D^{olivine/melt}$ for Ti, Cr, Ca, Al, and Mn, as was done in the section above. The $D^{olivine/melt}$ values used for these calculations are presented in Table 2. The assumption in these calculations is that olivine compositions were not greatly disturbed during subsolidus re-equilibration or transport in the 74275 magma. TiO_2 was estimated for the melt in equilibria with the cores of the olivine in the dunitic xenolith. Using the $D_{Ti}^{olivine/melt}$ from above, the TiO_2 concentration of the melt in equilibrium with the core olivine is approximately 2.4 wt%. Using the relationship between Fe-Mg $K_D^{olivine/melt}$ and TiO_2 (Longhi et al. 1978; Delano 1980; Longhi 1992), a Fe-Mg $K_D^{olivine/melt}$ of 0.32 was used to calculate the Mg# of melts in equilibrium with the olivine in the xenolith. Using the core olivine composition, the Mg# of melts in equilibrium olivine is approximately 58. The value is somewhat compromised in that the Mg# of individual olivine grains making up the xenolith was probably modified slightly in the magma chamber. Most likely, the Mg# may have been higher. These two calculated values suggest that the dunite represents a cumulate produced from the crystallization of a low-Ti mare basalt rather than the high-Ti basalt that carried it to the surface of the Moon. Therefore, the dunitic xenolith is a xenolith representing earlier olivine crystallization from an unrelated, low-Ti magma. Other melt characteristics calculated from the xenolith are Cr_2O_3 = 0.34 wt%, CaO = 7.85 wt%, Al_2O_3 = 5.40 wt%, and MnO = 0.19 wt%.

By plotting the Mg# and TiO_2 of the calculated xenolith parent melt composition on the LLD diagram (Fig. 7) modified from Longhi (1987), the relationship between this calculated magma and other lunar basalts may be examined. The calculated melt composition plots within the field of primitive low-Ti mare basalts at TiO_2 slightly below the values for the Apollo 14 (4.7 wt% TiO_2) and 15 (3.5 wt% TiO_2) yellow pyroclastic glasses. The Mg# is slightly higher than these glass compositions. The calculated LLD for this parental magma for the xenoliths intersect fields defined by the Apollo 12 pigeonite basalts and Apollo 12 ilmenite basalts. With the relatively low calculated incompatible major and minor elements (Cr, Ca, Al, and Mn) concentrations in the parental magma, crystallization of olivine along the projected LLD (Fig. 7) would result in these elements reaching concentrations typical of more evolved mare basalts. The LLD trajectory for this bulk composition also explains the absence of oxides and other minor phases in the xenolith; olivine is the only liquidus phase at these TiO_2 and Mg# values (Longhi 1987). An unusual characteristic of the olivines in the dunite xenolith and the calculated liquid composition is that they are both low in Ni and Co relative to many other low-Ti basalts (Fig. 6). The Ni and Co concentrations of the olivines in the xenolith are 100–200 and 40–80 ppm, respectively, whereas the cores of olivines in most low-Ti mare basalts with low Mg# are 400–700 and 200–300 ppm (Fig. 5) Ni and Co, respectively. Part of this difference is due to the slightly higher TiO_2 of the calculated parent melt compared to the low-Ti magmas that are presented in Fig. 5. As demonstrated by Delano (1986) and Shearer et al. (1996), Ni and Co in lunar pyroclastic glasses is general inversely correlated with Mg#. For example, very low-Ti glasses have Ni and Co 2–3 times higher (Ni = 90–200 ppm Ni) than low-Ti and intermediate-Ti pyroclastic glasses (Ni = 55–85 ppm). Still, even with the slightly higher TiO_2, the olivine and the calculated parent magma are lower in Ni and Co than expected for low-Ti mare basalts. It is therefore our conclusion that this dunite xenolith crystallized from a mare magma not sampled at either the Apollo 17 site or any of the other Apollo landing sites.

Thermal History and Transportation of the Xenoliths to the Lunar Surface

There are three thermal episodes recorded in the major and minor element zoning observed in olivine from

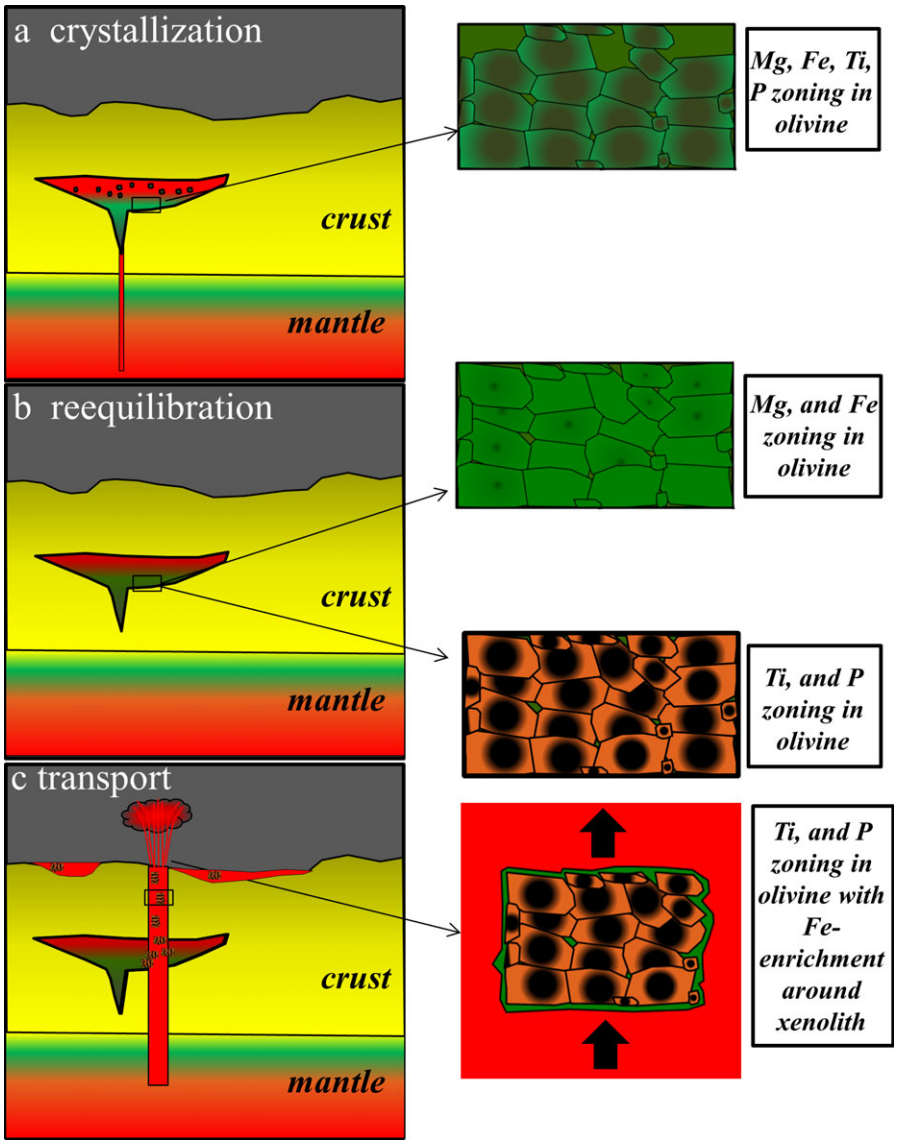

Fig. 9. Schematic of model for the petrogenesis of the dunite xenolith identified in 74275. a) Dunite layer in low-Ti mare basalt intrusion consisting of cumulate olivine zoned from high Mg# and low P and Ti cores to low Mg# and high P and Ti rims. The dunite lithology represented by sample 72415 originates closer to the crust–mantle boundary. b) At subsolidus temperatures, high $D^{Fe\text{-}Mg}$ results in creating Mg# homogeneity. The preservation of P and Ti zoning requires a slower D^{P} and D^{Ti} at these temperatures. c) Once incorporated as a xenolith in the 74275 high-Ti mare basalt, the P and Ti zoning in the cumulate olivine is preserved as a result of relatively rapid transport and eruption of the host magma. The xenolith reacts with host magma to form a thin rim (green) enriched in Fe, Ti, and P.

the xenolith (1) an event representing the crystallization from a low-Ti parent magma, (2) an event representing re-equilibration during either magmatic residence in the magma chamber or in the cumulate pile, and (3) an event representing re-equilibration during transport in the 74275 magma. These different episodes are superimposed on one another, but can be deconvolved (Fig. 9).

The P and Ti zoning observed in each individual olivine crystal making up the xenolith most likely represents the magmatic crystallization of the olivine from the low-Ti parent magma (Fig. 9a). The low concentration of P, Al, Ti, and perhaps V in the cores, with enrichments of these elements in the rims, is consistent with enrichment of the parent magma in incompatible elements during crystallization. However, this zoning is considerably different than the cryptic oscillatory style of P and Al zoning observed in many other olivines (Milman-Barris et al. 2008; Shearer et al. 2013; Elardo and Shearer 2014). The low-diffusivity of P and Al is consistent with the preservation of igneous

zoning during the olivine's postcrystallization thermal history (Milman-Barris et al. 2008; Shearer et al. 2013). The preservation of the corresponding Ti zoning has not been documented in many other igneous olivines (Milman-Barris et al. 2008) and is a bit more perplexing. Its preservation provides both constraints for the thermal history of the xenolith and the relative diffusivity of Ti in olivine at subsolidus temperatures.

Across the individual olivine crystals making up the xenolith and across the complete xenoliths (except the thin reaction rim around the whole xenolith), the Mg# is fairly constant (0.82–0.83) and is not correlated with the variation in Ti, Al, and P. Our interpretation of this homogenous Mg# is that it represents a postcrystallization re-equilibration of olivine making up the dunite xenolith. The diffusivity of Fe-Mg in olivine is several orders of magnitude faster than P. Therefore, the P igneous zoning is preserved, whereas the Mg# is not. In that the thin reaction rim appears to be the result of the interaction between the 74275 magma and xenolith, it is more likely that the re-equilibration of Mg and Fe occurred in the dunite cumulate pile. The occurrence of this subsolidus episode potentially causes a dilemma for the preservation of Ti (and perhaps V) zoning. Experimental diffusion studies of minor and trace elements in San Carlos olivine at 1300 °C (Spandler and O'Neill 2010) and examination of a mantle olivine xenocryst in a dioritic magma at 950 °C (Qian et al. 2010) have been interpreted as indicating Ti and V diffuse much faster than the corresponding Mg-Fe interdiffusion coefficient. However, more recent measurements indicate that Ti diffusivities in olivine are similar to those of trivalent REEs and considerably slower than those of Cr, Ca, and Fe-Mg in olivine (Cherniak and Liang 2014). Ilmenite exsolution in olivine from the Skaergaard intrusion, and the Cuillin Igneous Complex, Isle of Skye (Moseley 1981) implies that during long subsolidus cooling of these intrusions, Ti is mobile in olivine. The lack of these textures in the dunite xenolith suggests that the re-equilibration of the olivine occurred at relatively shallow- to midcrustal levels and on a time scale that was insufficient for the resetting of the Ti zoning profile

Based on the textures shown in Figs. 1, 2, and 3, the Fe-enriched reaction rim around the xenolith is clearly the result of the interaction between the 74275 basalt and the xenolith. These figures show that the Fe-enrichment is associated with the outer-most surface of the xenolith and not around individual olivine grains making up the xenolith. Using the methodology discussed above to decipher the Fe-enrichment associated with the rims of the megacryst, the postincorporation history of the xenolith may be calculated. Figure 8b compares the zoning profile of Mg# across the dunite xenolith to the zoning profile calculated using the approach of Costa et al. (2008). This comparison indicates that the xenolith was incorporated and transported in the 74275 magma over a period of time between 30 and 70 days.

CONCLUSIONS

Lunar basalt 74275 contains a complex population of olivine that consists of microphenocrysts, megacrysts, and dunitic xenoliths. Reconstruction of melt compositions and LLDs indicate that the microphenocrysts and megacrysts crystallized from a single high-Ti mare basalt magma under different conditions. The megacrysts crystallized earlier than the microphenocrysts in a magma chamber at hypabyssal crustal conditions. They were transported to the lunar surface in the 74275 basalt over a period of 30 days or less. The high-Ti basalt remained olivine saturated and at or near the surface the microphenocrysts crystallized from the magma. The dunite xenoliths do not represent deep crustal or shallow mantle lithologies. They are texturally and chemically distinct from other dunites identified from the Apollo 17 site. More likely, they represent olivine cumulates that crystallized from a low-Ti mare basalt at intermediate to shallow crustal levels. As indicated by numerous calculated chemical characteristics, the parent basalt to the dunite xenolith lithology was more primitive than low-Ti basalts thus far returned from the Moon. In addition, this parental magma, or its more evolved daughter magmas, was not collected on the surface of the Taurus-Littrow Valley by the Apollo 17 mission. The dunite lithology was exposed to several episodes of re-equilibration. During the last episode of re-equilibration (rim on the xenolith), the dunite cumulate was sampled by the 74275 magma and transported over a period of 30–70 days to the lunar surface.

In one of the few acknowledged occurrences of dunite xenoliths in lunar basalts, the lithology is concluded to originate from mid- to upper-crustal horizons. Although this study did not identify upper mantle mineral assemblages, there are other samples that could be examined for deep crustal and upper mantle lithologies. Ryder et al. (1997) identified both magnesian olivine (Fo_{90-94}) and orthopyroxene (En_{90-84} $Wo_{1.3}$) in poikilitic melt breccias that were produced during the Serenitatis impact event. Some of the minor element characteristics (e.g., TiO_2) of the magnesian olivine and orthopyroxene are distinctly different from highlands plutonic rocks (Ferroan Anorthosites, Mg-suite). Between 1970 and 1976, the Luna robotic sample return program carried out by the Soviet Union collected drill cores along a ~480 km "traverse" from the Fecunditatis basin (Luna 16) to the lunar highlands between the Fecunditatis and Crisium basins (Luna 20) to the Crisium

basin (Luna 24). The total mass of the cores that were returned was approximately 321 g with Luna 16 returning ~101 g, Luna 20 returning ~50 g, and the Luna 24 returning ~170 g. Approximately 12 g of material from these missions was received by NASA with smaller portions allocated to the Royal Society of London and India. Of particular interest are the Luna 20 samples. In the NASA sample allocation, magnesium-rich olivines and pyroxenes occur with crystalline rocks and mineral fragments. Olivine has compositions up to Fo_{94} and the orthopyroxene have magnesium-rich compositions of $Wo_{03}En_{85}Fs_{12}$ (Cameron et al. 1973; Ghose et al. 1973). The petrologic heritage of these mineral fragments is unknown. Reexamination of the NASA allocated samples and the entire Luna sample collection could be extremely valuable in identifying materials from the deep lunar crust and upper mantle.

To close, it is still puzzling that in light of large impact basins that produce a thin crust (Wieczorek and Phillips 1998; Wieczorek et al. 2006, 2013) and presumably excavated mantle in several impact basins (Wieczorek et al. 2006, 2013; Melosh et al. 2014; Miljkovic et al. 2015) that deep crustal mineral assemblages are somewhat rare and mantle assemblages have not been unambiguously identified in the lunar sample collection. There are several potential reasons for this ambiguity. The simplest explanation is that the sample collection (Apollo and Luna programs, lunar meteorites) does not adequately represent terrains that may contain excavated mantle (e.g., Yamamoto et al. 2010; Melosh et al. 2014). Alternatively, the upper lunar mantle is considerably different than is currently envisioned and therefore it has not been recognized in the sample collection. For example, Melosh et al. (2014) suggested that the upper mantle is dominated by orthopyroxene rather than olivine. There are interpretive issues tied to the remote sensing data on which many of these conclusions are based. Both olivine and orthopyroxene identified on the lunar surface by orbital missions could be derived from crustal rather than mantle sources. Finally, one must consider the possibility that large impacts that formed basins on the Moon do not necessarily penetrate the crust and excavate the mantle. In an analysis of ejecta deposits associated with the Orientale Basin (approximately 1000 km in diameter), Spudis and Martin (2014) concluded that only the upper crust was excavated. However, other basins such as South Pole–Aitken and Imbrium basins clearly excavated more mafic, varied, and deeper crustal–mantle regions (Melosh et al. 2014; Spudis and Martin 2014) that may have transported mantle material to the lunar surface. Further exploration of these basins with a continued reassessment of samples in hand and future targeted sample return may help resolve this dilemma.

Acknowledgments—The authors thank Brad Jolliff and Rachel Klima for their insightful reviews that substantially improved this manuscript. Associate editor Carle Pieters provided useful comments and timely reviews. CKS acknowledges support from the NASA Cosmochemistry Program and the NASA Lunar Advanced Science for Exploration Research Program during this study (Grant no. NNX13AH85G and NNX13AJ58G to CKS). CRN was supported by subcontract 02235-05 from NASA SSERVI contract NNA14AB07A (PI D. Kring). We are indebted to Yunbin Guan, California Institute of Technology, and the Caltech Microanalysis Center (CMC) for providing access to the ion microprobe facility.

Editorial Handling—Dr. Carle Pieters

REFERENCES

Anderson A. T. Jr. 1983. Oscillatory zoning of plagioclase: Nomarski interference contrast microscopy of etched sections. *American Mineralogist* 68:125–129.

Andre C. G., Wolfe R. W., and Adler I. 1978. Evidence for a high-magnesium subsurface basalt in Mare Crisium from orbital x-ray fluorescence data. In *Mare Crisium: The view from Luna 24*, edited by Merrill R. B. and Papike J. J. *Geochimica et Cosmochimica Acta* Suppl. 9:1–12.

Armienti P., Pareschi M. T., Innocenti F., and Pompilio M. 1994. Effects of magma storage and ascent on the kinetics of crystal growth. *Contributions to Mineralogy and Petrology* 115:402–414.

Basaltic Volcanism Study Project 1981. *Basaltic volcanism on the terrestrial planets*. New York: Pergamon. 1286 p.

Basu A., McKay D. S., and Fruland R. M. 1978. Origin and modal petrology of Luna 24 soils. In *Mare Crisium: The view from Luna 24*, edited by Merrill R. B. and Papike J. J. *Geochimica et Cosmochimica Acta* Suppl. 9: 321–337.

Beaty D. W. and Albee A. L. 1980. The petrology of a pyroxenite xenolith in mare basalt 10050. Proceedings, 11th Lunar and Planetary Science Conference. pp. 67–69.

Bell P. M. and Mao H. K. 1975. Cataclastic plutonics: Possible keys to the evolutionary history of the early Moon. Proceedings, 6th Lunar Science Conference. pp. 34–35.

Bell A. S., Burger P. V., Le L., Papike J. J., Jones J., and Shearer C. K. 2014. Chromium oxidation state in planetary basalts: Oxygen fugacity indicator and critical variable for Cr-spinel stability (abstract #1777). 45th Lunar and Planetary Science Conference. CD-ROM.

Blanchard D. P., Brannon J. C., Aaboe E., and Budahn J. R. 1978. Major and trace element chemistry of Luna 24 samples from Mare Crisium. In *Mare Crisium: The view from Luna 24*, edited by Merrill R. B. and Papike J. J. *Geochimica et Cosmochimica Acta* Suppl. 9:613–630.

Blundy J. D. and Shimizu N. 1991. Trace element evidence for plagioclase recycling in calc-alkaline magmas. *Earth and Planetary Science Letters* 102:178–197.

Bottinga Y., Kudo A., and Weill D. 1966. Some observations on oscillatory zoning and crystallization of magmatic plagioclase. *American Mineralogist* 51:792–806.

Brown G. M., Peckett A., Emeleus C. H., Phillips R., and Pinsent R. H. 1975. Petrology and mineralogy of Apollo

17 mare basalts. Proceedings, 6th Lunar Science Conference. pp. 1–13.
Butler P. 1972. Compositional characteristics of olivine from Apollo 12 samples. *Geochemica et Cosmocheimica Acta* 36:773–785.
Cameron K. L., Papike J. J., Bence A. E., and Sueno S. 1973. Petrology of fine-grained rock fragments and petrologic implications of single crystals from the Luna 20 soil. *Geochemica et Cosmocheimica Acta* 37:775–794.
Cashman K. V. and Marsh B. D. 1988. Crystal size distribution (CSD) in rocks and the kinetics and dynamics of crystallization. *Contributions to Mineralogy and Petrology* 99:292–305.
Chakraborty S. 1997. Rates and mechanisms for Fe-Mg interdiffusion in olivine at 980°C–1300°C. *Journal of Geophysical Research* 102:12,317–12,331.
Chakraborty S. 2010. Diffusion coefficients in olivine, wadsleyite, and ringwoodite. In *Diffusion in minerals and melts*, edited by Zhang Y. and Cherniak D. J. Reviews in Mineralogy and Geochemistry, vol. 72. Washington, D.C.: Mineralogical Society of America. pp. 603–640.
Cherniak D. J. and Liang Y. 2014. Titanium diffusion in olivine. *Geochimica et Cosmochimica Acta* 147:43–57.
Colson R. O., Mckay G. A., and Taylor L. A. 1988. Temperature and composition dependencies of trace-element partitioning—olivine melt and low-Ca pyroxene melt. *Geochimica et Cosmochimica Acta* 52:539–553. doi:10.1016/0016-7037(88)90109-3.
Corley L. M., McGovern P. J., and Kramer G. Y. 2014. Olivine exposures on the Moon: Origins and mechanisms of transport to the lunar surface (abstract #1564). 45th Lunar and Planetary Conference. CD-ROM.
Costa F. and Dungan M. 2005. Short time scales of magmatic assimilation from diffusion modeling of multiple elements in olivine. *Geology* 33:837–840.
Costa F., Cohmen R., and Chakrabortzry S. 2008. Time scales of magmatic processes from modeling the zoning patterns of crystals. In *Minerals, inclusions, and volcanic processes*, edited by Putirka K. D. and Tepley F. J. Reviews in Mineralogy and Geochemistry vol. 69. Washington, D.C.: Mineralogical Society of America. pp. 545–594.
Day J. M. D. and Taylor L. A. 2007. On the structure of mare basalt lava flows from textural analysis of the LaPaz Icefield and Northwest Africa 032 lunar meteorities. *Meteoritics & Planetary Science* 42:3–17.
Delano J. W. 1980. Chemistry and liquidus relations of Apollo 15 red glass: Implications for the deep lunar interior. Proceedings, 11th Lunar and Planetary Science Conference. pp. 251–288.
Delano J. W. 1986. Pristine lunar glasses: Criteria, data and implications. Proceedings 16th Lunar and Planetary Science Conference. *Journal Geophysical Research* 91:D201–D213.
Delano J. W. and Lindsley D. H. 1982. Chromium, nickel, and titanium abundances in 74275 olivines: More evidence for a high-pressure origin of high-titanium mare basalts. Proceedings, 13th Lunar and Planetary Science Conference. pp. 160–161.
Donaldson C. H. 1976. An experimental investigation of olivine morphology. *Contributions to Mineralogy and Petrology* 57:187–213.
Duncan A. R., Erlank A. J., Willis J. P., Sher M. K., and Ahrens L. H. 1974. Trace element evidence for a two-stage origin of some titaniferous mare basalts. Proceedings, 5th Lunar Science Conference. pp. 1147–1157.
Dunn T. 1987. Partitioning of Hf, Lu, Ti, and Mn between olivine, clinopyroxene and basaltic liquid. *Contributions to Mineralogy and Petrology* 96:476–484.
Dymek R. F., Albee A. L., and Chodos A. A. 1975. Comparative petrology of lunar cumulate rocks of possible primary origin: Dunite 72415, troctolite 76535, norite 78235, and anorthosite 62237. Proceedings, 6th Lunar Science Conference. pp. 301–341.
El Goresy A., Ramdohr P., Medenbach O., and Bernhardt H.-J. 1974. Taurus-Littrow TiO_2-rich basalts: Opaque mineralogy and geochemistry. Proceedings, 5th Lunar Science Conference. pp. 627–652.
Elardo S. M. and Shearer C. K. 2014. Magma chamber dynamics recorded by oscillatory zoning in pyroxene and olivine phenocrysts in basaltic lunar meteorite Northwest Africa 032. *American Mineralogist* 99:355–368.
Fagan T. J., Taylor G. J., Keil K., Bunch T. E., Wittke J. H., Korotev R. L., Jolliff B. L., Gillis J. J., Haskin L. A., Jarosewich E., Clayton R. N., Mayeda T. K., Fernandes V. A., Burgess R., Turner G., Eugster O., and Lorenzetti S. 2002. Northwest Africa 032: Product of lunar volcanism. *Meteoritics & Planetary Science* 37:371–394.
Gaetani G. A. and Grove T. L. 1997. Partitioning of moderately siderophile elements among olivine, silicate melt, and sulfide melts: Constraints on core formation in the Earth and Mars. *Geochimica et Cosmochimica Acta* 61:1829–1846.
Ghose S., McCallum L. S., and Tidy E. 1973. Luna 20 pyroxenes: Exsolution and phase transformation as indicators of petrologic history. *Geochemica et Cosmocheimica Acta* 37:831–839.
Green D. H., Ringwood A. E., Hibberson W. O., and Ware N. G. 1975. Experimental petrology of Apollo 17 mare basalts. Proceedings, 6th Lunar Science Conference. pp. 871–893.
Hanson B. and Jones J. H. 1998. The systematics of Cr^{3+} and Cr^{2+} partitioning between olivine and liquid in the presence of spinel. *American Mineralogist* 83:669–684.
Hodges F. N. and Kushiro I. 1974. Apollo 17 petrology and experimental determination of differentiation sequences in model Moon compositions. Proceedings, 5th Lunar Science Conference. pp. 505–520.
Huneke J. C., Jessberger E. K., Podosek F. A., and Wasserburg G. J. 1973. $^{40}Ar/^{39}Ar$ measurements in Apollo 16 and 17 samples and the chronology of metamorphic and volcanic activity in the Taurus-Littrow region. Proceedings, 4th Lunar Science Conference. pp. 1725–1756.
Husain L. and Schaeffer O. A. 1973. Lunar volcanism: Age of the glass in the Apollo 17 orange soil. *Science* 180:1358–1360.
Jerram D. A., Cheadle M. J., and Philpotts A. J. 2003. Quantifying the building blocks of igneous rocks: Are clustered crystal frameworks the foundation? *Journal of Petrology* 44:2033–2051.
Kohler T. P. and Brey G. P. 1990. Calcium exchange between olivine and clinopyroxene calibrated as a geothermobarometer for natural peridotites from 2 to 60 kb with applications. *Geochimica et Cosmochimica Acta* 54:2375–2388.
Kuskov O. L., Kronrod V. A., and Kronrod E. V. 2015. Thermochemical constraints on the thermal state, composition, and mineralogy of the upper mantle of the Moon: Evidence from the seismic models. *Solar System Research* 49:75–91.
Lindstrom D. J. 1983. Kinetic effects on trace element partitioning. *Geochimica et Cosmochimica Acta* 47:617–622. doi:10.1016/0016-7037(83)90282-X.

Lofgren G. 1972. Temperature induced zoning in synthetic plagioclase feldspar. In *The feldspars*, edited by MacKenzie W. S. Manchester, UK: University of Manchester Press. pp. 367–377.

Longhi J. 1987. On the connection between mare basalts and picritic volcanic glasses. Proceedings, 17th Lunar and Planetary Science Conference. *Journal of Geophysical Research* 92:E349–E360.

Longhi J. 1992. Experimental petrology and petrogenesis of mare volcanics. *Geochimica et Cosmochimica Acta* 56:2235–2251.

Longhi J., Walker D., and Hays J. F. 1978. The distribution of Fe and Mg between olivine and lunar basaltic liquids. *Geochimica et Cosmochimica Acta* 42:1545–1558.

Mallmann G. and O'Neill H. St. C. 2009. The crystal/melt partitioning of V during mantle melting as a function of oxygen fugacity compared with some other elements (Al, P, Ca, Sc, Ti, Cr, Fe, Ga, Y, Zr and Nb). *Journal of Petrology* 50:1765–1794.

Marsh B. D. 1998. On the interpretation of crystal size distributions in magmatic systems. *Journal of Petrology* 39:553–599.

Marvin U. B., Carey J. W., and Lindstom M. M. 1989. Cordierite-spinel troctolite, a new magnesium-rich lithology from the lunar highlands. *Science* 243:925–928.

McCallum I. S. and Schwartz J. M. 2001. Lunar Mg-suite: Thermobarometry and petrogenesis of parental magmas. *Journal of Geophysical Research* 106(E11):27969–27983.

McGetchin T. R. and Ullrich G. W. 1973. Xenoliths in maars and diatremes with inferences for the Moon, Mars, and Venus. *Journal of Geophysical Research* 78:1833–1853.

McKenzie D. and O'Nions R. K. 1991. Partial melt distributions from inversion of rare-earth element concentrations. *Journal of Petrology* 32:1021–1042.

Melosh H. J., Kendall J., Johnson B. C., Bowling T., Horgan B., Lucey P. G., and Taylor G. J. 2014. The Moon's upper mantle: Mostly opx, not olivine? (abstract #2505). 45th Lunar and Planetary Science Conference. CD-ROM.

Meyer C. E. and Wilshire H. G. 1974. "Dunite" inclusion in lunar basal 74275 (abstract). 5th Lunar Science Conference. p. 503.

Mikouchi T., McKay G., and Le L. 1994. Cr, Mn, and Ca distributions for olivine in angritic systems: Constraints on the origins of Cr-rich and Ca-poor core olivine in angrite LEW 87051. Proceedings, 25th Lunar and Planetary Science Conference. pp. 907–908.

Miljkovic K., Wieczorek M. A., Collins G. S., Solomon S. C., Smith D. E., and Zuber M. T. 2015. Excavation of the lunar mantle by basin-forming impact events on the Moon. *Earth and Planetary Science Letters* 409:243–251.

Milman-Barris M., Beckett J. R., Baker M. B., Hofmann A. E., Morgan Z., Crowley M., Vielzeuf D., and Stolper E. M. 2008. Zoning of phosphorus in magmatic olivine. *Contributions to Mineralogy and Petrology* 155:739–765. doi:10.1007/s00410-007-0268-7.

Miyamoto M., Koizuma E., and Mikouchi T. 2006. Verification of a model to calculate cooling rates in olivine by consideration of Fe-Mg diffusion and olivine crystal growth II (abstract #1538). 37th Lunar and Planetary Science Conference. CD-ROM.

Moores E. M. 1982. Origin and emplacement of ophiolites. *Reviews of Geophysics* 20:735–760.

Moseley D. 1981. Ilmenite exsolution in olivine. *American Mineralogist* 66:976–979.

Murthy V. R. and Coscio C. 1977. Rb-Sr isotopic systematics and initial Sr considerations for some lunar samples (abstract). Proceedings, 8th Lunar Science Conference. p. 706.

Neal C. R. and Taylor L. A. 1992. Petrogenesis of mare basalts: A record of lunar volcanism. *Geochimica et Cosmochimica Acta* 56:2177–2211.

Neal C. R. and Taylor L. A. 1993. *Catalog of Apollo 17 rocks. Vol. 3 Central Valley*. Houston, Texas: Curators Office LBJSC.

Neal C. R., Taylor L. A., Patchen A. D., Hughes S. S., and Schmitt R. A. 1990. The significance of fractional crystallization in the petrogenesis of Apollo 17 Type A and B high-Ti basalts. *Geochimica et Cosmochimica Acta* 54:1817–1833.

Nikogosian I. K. and Sobolev A. V. 1997. Ion-microprobe analysis of melt inclusions in olivine: experience in estimating the olivine-melt partition coefficients of trace elements. *Geochemical International* 35:119–126.

Nunes P. D., Tatsumoto M., and Unruh D. M. 1974. U-Th-Pb systematics of some Apollo 17 lunar samples and implications for a lunar basin excavation chronology. Proceedings, 5th Lunar Science Conference. pp. 1487–1514.

Nyquist L. E., Bansal B. M., and Wiesmann H. 1976. Sr isotopic constraints on the petrogenesis of Apollo 17 mare basalts. Proceedings, 7th Lunar Science Conference. pp. 1507–1528.

Onorato P. I. K., Uhlmann D. R., Taylor L. A., Coish R. A., and Gamble R. P. 1978. Olivine cooling speedometers. Proceedings, 9th Lunar and Planetary Science Conference. pp. 613–628.

Paces J. B., Nakai S., Neal C. R., Taylor L. A., Halliday A. N., and Lee D.-C. 1991. A strontium and neodymium isotopic study of Apollo 17 high-Ti mare basalts: Resolution of ages, evolution of magmas, and origin of source heterogeneities. *Geochimica et Cosmochimica Acta* 55:2025–2043.

Papike J. J., Bence A. E., and Lindsley D. H. 1974. Mare basalts from the Taurus-Littrow region of the Moon. Proceedings, 5th Lunar Science Conference. pp. 471–504.

Papike J. J., Hodges F. N., Bence A. E., Cameron M., and Rhodes J. M. 1976. Mare basalts: Crystal chemistry, mineralogy and petrology. *Reviews of Geophysics and Space Physics* 14:475–540.

Papike J. J., Ryder G., and Shearer C. K. 1998. Lunar samples. *Reviews in Mineralogy* 36:51–5234.

Powell K. E., McGovern P. J., and Kramer G. Y. 2012. Olivine detections at the rim of Crisium basin with Moon Mineralogical Mapper (abstract #1689). 43rd Lunar and Planetary Conference. CD-ROM.

Qian Q., O'Neill H. St. C., and Hermann J. 2010. Comparative diffusion coefficients of major and trace elements in olivine at ~950°C from a xenocryst included in dioritic magma. *Geology* 38:331–334.

Quick J. E. 1981. Petrology and petrogenesis of the Trinity peridotite. *Journal of Geophysical Research* 86:11,837–11,863.

Rhodes J. M., Hubbard N. J., Wiesmann H., Rodgers K. V., Brannon J. C., and Bansal B. M. 1976. Chemistry, classification, and petrogenesis of Apollo 17 mare basalts. Proceedings, 7th Lunar Science Conference. pp. 1467–1489.

Ryder G. 1988. Quenching and disruption of lunar KREEP lava flows by impacts. *Nature* 336:751–754.

Ryder G. 1990. A distant variant of high-titanium mare basalt from the Van Serg Core, Apollo 17 landing site. *Meteoritics* 25:249–258.

Ryder G. 1992. Chemical variation and zoning of olivine in lunar dunite 72415: Near-surface accumulation. Proceedings, 22nd Lunar and Planetary Science Conference. pp. 373–380.

Ryder G. and Marvin U. B. 1978. On the origin of Luna 24 basalts and soils. In *Mare Crisium: The view from Luna 24*, edited by Merrill R. B. and Papike J. J. Oxford: Pergamon. pp. 339–355.

Ryder G., Norman M. D., and Taylor G. J. 1997. The complex stratigraphy of the highland crust in the Serenitatis region of the Moon inferred from mineral fragment chemistry. *Geochimica et Cosmochimica Acta* 61:1083–1105.

Shearer C. K. and Papike J. J. 2005. Early crustal building processes on the Moon: Models for the petrogenesis of the Mg-suite. *Geochimica et Cosmochimica Acta* 69:3445–3461.

Shearer C. K., Papike J. J., and Layne G. D. 1996. Deciphering basaltic magmatism on the Moon from the compositional variations in the Apollo 15 very low-Ti picritic magmas. *Geochimica et Cosmochimica Acta* 60:509–528.

Shearer C. K., Hess P. C., Wieczorek M. A., Pritchard M. E., Parmentier E. M., Borg L. E., Longhi J., Elkins-Tanton L. T., Neal C. R., Antonenko I., Canup R. M., Halliday A. N., Grove T. L., Hager B. H., Lee D.-C., and Wiechert U. 2006. Chapter 3. Magmatic and thermal history of the Moon. In *New views of the moon*, edited by Jolliff B., Wieczorek M., Shearer C. K., and Neal C. Reviews in Mineralogy and Geochemistry, vol. 60. Washington, D.C.: Mineralogical Society of America. pp. 365–518.

Shearer C. K., Burger P. V., Papike J. J., Borg L. E., Irving A. J., and Herd C. 2008. Petrogenetic linkages among martian basalts. Implications based on trace element chemistry of olivine. *Meteoritics & Planetary Science* 43:1241–1258.

Shearer C. K., Aaron P. M., Burger P. V., Guan Y., Bell A., and Papike J. J. 2013. Petrogenetic linkages among fO_2, isotopic enrichments-depletions and crystallization history in martian basalts. Evidence from the distribution of phosphorus in olivine megacrysts. *Geochimica et Cosmochimica Acta* 120:17–38.

Shearer C. K., Elardo S. M., Petro N. E., Borg L. E., and McCubbin F. M. 2015. Origin of the lunar highlands Mg-suite plutonic rocks: An integrated petrology, geochemistry, chronology, and remote sensing perspective. *American Mineralogist* 100:294–325.

Shimizu N., Semet M. P., and Allgre C. J. 1978. Geochemical applications of quantitative ion-microprobe analysis. *Geochimica et Cosmochimica Acta* 42:1321–1334.

Simkin T. and Smith J. V. 1970. Minor-element distribution in olivine. *The Journal of Geology* 78:304–325.

Spandler C. and O'Neill H. St. C. 2010. Diffusion and partition coefficients of minor and trace elements in San Carlos olivine at 1,300°C with some geochemical implications. *Contributions to Mineralogy and Petrology* 159:791–818.

Spera F. J. 1992. Lunar magma transport phenomena. *Geochimica et Cosmochimica Acta* 56:2253–2266.

Spudis P. D. and Martin D. J. P. 2014. Composition of the deposits of the lunar Orientale Basin (abstract #1469). 45th Lunar and Planetary Science Conference. CD-ROM.

Spudis P. D., Ryder G., Taylor G. J., McCormick K. A., Keil K., and Grieve R. A. F. 1991. Sources of mineral fragments in impact melts, 15445 and 15455: Toward the origin of low-K Fra mauro basalt. Proceedings, 21st Lunar and Planetary Science Conference. pp. 151–165.

Sung C.-M., Abu-Eid R. M., and Burns R. G. 1974. Ti^{3+}/Ti^{4+} ratios in lunar pyroxenes: implications to depth of origin of mare basalt magma. Proceedings, 5th Lunar Science Conference. pp. 717–726.

Taura H., Yurimoto H., Kurita K., and Sueno S. 1998. Pressure dependence on partition coefficients for trace element between olivine and the coexisting melts. *Physics and Chemistry of Minerals* 25:469–484.

Taylor G. J., Warren P. H., Ryder G., Pieters C., and Lofgren G. 1991. Lunar rocks. In *Lunar source book: A user's guide to the Moon*, edited by Heiken G. H., Vaniman D. T., and French B. V. Cambridge: Cambridge University Press. pp. 183–284.

Walker D., Longhi J., Grove T., Stolper E., and Hays J. F. 1973. Experimental petrology and origin of rocks from the Descartes highlands. Proceedings, 4th Lunar Science Conference. pp. 1013–1032.

Walker D., Longhi J., and Hays J. F. 1975a. Heterogeneity in titaniferous lunar basalts. In *Conference on origins of mare basalts and their implications for lunar evolution*. Houston, Texas: Lunar Science Institute. pp. 169–173.

Walker D., Longhi J., Stolper E. M., Grove T. L., and Hays J. F. 1975b. Origin of titaniferous lunar basalts. *Geochimica et Cosmochimica Acta* 39:1219–1235.

Walker D., Longhi J., and Hays J. F. 1976. Heterogeneity in titaniferous lunar basalts. *Earth and Planetary Science Letters* 30:27–36.

Warner R. D., Keil K., Murali A. V., and Schmitt R. A. 1975. Petrogenetic relationships among Apollo-17 basalts. In *Papers presented to the conference on origins of mare basalts and their implications for lunar evolution*. Houston, Texas: Lunar Science Institute. pp. 179–183.

Wieczorek M. A. and Phillips R. J. 1998. Potential anomalies on a sphere: Application to the thickness of the lunar crust. *Journal of Geophysical Research* 103:1715–1724.

Wieczorek M. A., Jolliff B. L., Khan A., Prichard M. E., Weiss B. P., Williams J. G., Hood L. I., Righter K., Neal C. R., Shearer C. K., McCallum I. S., Tompkins S., Hawke B. R., Peterson C., Gillis J. J., and Bussey B. 2006. Lunar interior constitution and structure. In *New views of the Moon*, edited by Jolliff B., Wieczorek M., Shearer C. K. and Neal C. Reviews in Mineralogy and Geochemistry, vol. 60. Washington, D.C.: Mineralogical Society of America. pp. 221–364.

Wieczorek M. A., Neumann G. A., Nimmo F., Kiefer W. S., Taylor G. J., Melosh H. J., Phillips R. J., Solomon S. C., Andrews-Hanna J. C., Asmar S. W., Konopliv A. S., Lemoine F. G., Smith D. E., Watkins M. W., Williams J. G., and Zuber M. T. 2013. The crust of the Moon as seen by GRAIL. *Science* 339:671–675.

Wilson L. and Head J. W. 1981. Ascent and eruption of basaltic magmas on the Earth and Moon. *Journal of Geophysical Research* 86:2971–3001.

Yamamoto S., Nakamura R., Matsunaga T., Ogawa Y., Ishihara Y., Morota T., Hirata N., Ohtake M., Hiroi T., Yokota Y., and Haruyama J. 2010. Possible mantle origin of olivine around lunar impact basins detected by SELENE. *Nature Geoscience* 3:533–536.